Grid cells implement a location-dependent directional code

Klara Gerlei[1], Jessica Passlack[1], Holly Stevens[1], Ioannis Papastathopoulos[3, 4], Matthew F. Nolan[1,2]

Affiliations: [1]Centre for Discovery Brain Sciences, [2]Simons Initiative for the Developing Brain, University of Edinburgh, Edinburgh, United Kingdom. EH8 9XD, [3]School of Mathematics, Maxwell Institute and Centre for Statistics, University of Edinburgh, United Kingdom. EH9 3FD, [4]The Alan Turing Institute, 96 Euston Road, London, NW1 2DB.

Grid and head direction codes in the medial entorhinal cortex represent cognitive spaces for navigation and memory [1,2]. In grid cells the expression of the grid code is thought to be independent of head direction, whereas in conjunctive cells the grid code is tuned to a single head direction [3]. This distinction between non-directional grid cells and unidirectional conjunctive cells is also present in models and proposed functions for grid codes [4–11]. However, while grid cells are not tuned to a single direction, whether their firing is independent of direction is less clear. Here we demonstrate location-dependent modulation of grid cell firing by head direction. Individual firing fields recorded from mouse and rat grid cells have multiple and different preferred directions. This local directionality of grid firing is accounted for by models in which grid cells integrate inputs from conjunctive cells with co-aligned, spatially non-uniform firing fields. Thus, the firing of grid cells is consistent with their integration of upstream grid codes. For downstream neurons in the dentate gyrus that receive input from grid cells, integration of rich directional information within the grid code may contribute to pattern separation computations by decorrelating different points of view from the same spatial location [12–14].

Grid codes are thought to provide a metric for spatial and conceptual representations used for navigation, learning and memory [1,15,16]. In the spatial domain grid codes have six-fold rotational symmetry, with individual fields appearing as the vertices of tessellating triangles that tile the floor of an environment [15]. Grid codes are generated by two functionally defined cell types found in the medial entorhinal cortex (MEC). Grid cells have grid firing fields that are thought to lack selectivity for head direction or other navigational variables [3,17]. In contrast, conjunctive cells have grid fields that manifest only when an animal moves in a particular direction [3]. Established models for grid firing assume that neurons with grid fields have either an absence of directional

tuning, as suggested for grid cells, or selectivity for a single direction, as described for conjunctive cells [4,5,8–10,18]. Analyses of the coding properties of grid cells make similar assumptions [6,7]. The possibility that grid cell activity is modulated by head direction, but in a manner that is qualitatively distinct from the directional tuning of conjunctive cells has received little attention.

To investigate directionality of grid cell firing we recorded from 324 neurons in the medial entorhinal cortex (MEC) of 15 mice across 179 recording sessions (2 - 16 sessions per animal, mean = 11.2, SD = 4.1 sessions). We identified 12 % of the recorded neurons (38 / 324) as having grid-like spatial firing fields using a metric based on the rotational symmetry of the autocorrelogram of their firing rate map [15] (see Methods). Evaluation of the directional firing of these neurons, using a metric that detects directional bias (see Methods), identified conjunctive cells, which were tuned to a single heading direction (n = 4), and grid cells (n = 34), which across the whole environment were active during head orientation in all directions (Extended Data). Because a low directional bias might nevertheless be compatible with a neuron encoding multiple directions, we compared the distribution of head directions when action potentials fired with the distribution of directions throughout the animal's trajectory (Figure 1a-c). The differences were significant for all grid cells (p < 0.001, n = 34, two-sample Watson U^2 test) arguing against the null hypothesis of independence between grid cell firing and head direction (Figure 1b-c). This directional firing was correlated between the first and second half of recording sessions indicating that it is stable over time (Figure S1). Analyses of grid cells recorded previously from rats (n=68)[3] gave similar results (Figure 1a-c).

To better understand the apparent directionality of grid cell firing, and because the Watson U^2 test would not rule out directional bias that could be introduced through variation in the time animals spend in different parts of a firing field (cf. [19]), we compared experimental recordings of spike rate binned by the animal's head direction with data that was shuffled while maintaining the location-dependent average firing rate (Figure 1d and Figure S2). For almost all grid cells, the number of directional bins in which the mean rate was outside the 95% confidence interval for the shuffled distribution was greater than expected given the shuffled data (p < 10^{-16} for mice and rats, Mann-Whitney U test)(Figure 1e). When we tested whether the experimental rate for each bin differed significantly from the shuffled data (threshold p < 0.05 after correcting for multiple comparisons made across bins), we found 7.3 ± 3.9 and 4.1 ± 4.5 significant bins / cell for mice and rats respectively (Figure 1e). Significant bins were found at peaks and troughs in

the firing rate histograms, which did not show clear unimodal tuning observed for conjunctive cells (cf. [3]). The orientation of the peaks differed substantially between grid cells indicating that they were not driven by common external cues (Figure S3). Variation in running speed between different parts of the environment is also unlikely to account for directional tuning as firing of most grid cells was independent from running speed (Extended Data). Together, these analyses indicate that firing of grid cells has directional structure that is qualitatively distinct from the unidirectional tuning of conjunctive cells.

If firing by grid cells encodes head direction then we expect this to also manifest at the level of individual firing fields. We therefore isolated spikes from each field using a watershed algorithm (44 fields isolated from 13 grid cells in 4 mice and 83 fields from 25 grid cells in 5 rats)(Figure 2a) and analysed directional firing separately for each field (Figure 2b-c). Directional histograms for single fields demonstrated clearer peaks than for the arena as a whole suggesting a greater degree of directional modulation at smaller spatial scales (cf. Figure 1a and 2b). When firing was binned by head direction (Figure 2x), we found that for experimental data the number of bins outside the 95 % confidence intervals of the corresponding shuffled distribution differed substantially from the number expected from the shuffled data (for mice and rats $p < 10^{-16}$, Mann-Whitney U test)(Figure 2e), and many bins differing significantly from the shuffled data (mice: 4.3 ± 3.2 bins / cell; rats: 2.1 ± 2.8 bins / cell, for mice and rats $p < 10^{-16}$ vs shuffled data)(Figure 2d). Directional modulation was correlated between the first and second half of each recording session indicating that it is stable at behaviourally relevant time scales (Figure S4). Because shuffled data maintained the position-dependent firing rate (Figure S2), the directional modulation could not be explained by the distributive hypothesis, which predicts directional modulation on the basis of time spent in different parts of the firing field [19]. Thus, directional modulation of grid cell firing manifests at the level of individual firing fields.

Inspection of individual fields from the same cell suggests that their directional modulation differs from one another (Figure 2b). Consistent with this, fields from grid cells did not on average show any correlation in their directional firing (median correlation for mice: -0.02 ± 0.3; for rats: 0.1 ± 0.3)(Figure 3a-b). This lack of correlation appeared not to be a result of undersampling of the field as correlations between fields from similarly sampled conjunctive cells were clearly detectable (median correlation for mice: 0.9 ± 0; rats: 0.6 ± 0.1)(Figure 3a-b). Furthermore, when comparing fields from the first and second half of the recording session correlations were detectable for the same field, but again were absent between different fields

(Figure 3c and Figure S5). Directional firing remained uncorrelated between fields when considering only fields adjacent to the walls of the arena, or only fields in the centre of the arena, indicating that the location dependence of directional tuning is also not related to the proximity of fields to the borders of the arena (Figure 3d). As directional modulation within each grid field is independent of direction modulation of other fields from the same grid cell, these data indicate that directional modulation of grid cell firing is location specific.

Our analyses imply that spatially specific multi-directional firing is a core feature of the grid code. This feature is not predicted by existing models for grid firing [5,8–10,18,20] (Supplemental Table 1). For example, a requirement of many continuous attractor models is that each grid cell has a single preferred direction of input [8,10]. An alternative possibility is that grid cell firing fields are generated through summation of inputs from co-aligned conjunctive cells [21]. While summation of spatially uniform conjunctive cell fields is insufficient to explain the directional biases of individual grid fields [21], recent analyses suggest that for a given grid cell its individual fields have large and stable differences in their amplitude [22]. We reasoned that incorporating this non-uniformity into the grid fields of conjunctive cells might allow integration of conjunctive cell inputs to account for the directionality of grid firing. In this case each of a grid cell's fields would be driven by input from a different combination of conjunctive cells with different head direction preferences. This scheme is consistent with projections from deeper layers of MEC, where conjunctive cells are found, to superficial layers where a greater proportion of grid cells are found [3,21,23].

To explore this idea we built models in which co-aligned theoretical conjunctive cell firing fields were convolved with experimentally recorded movement trajectories to generate spatially non-uniform conjunctive cell firing patterns (Figure 4a). Spike times from the simulated conjunctive cells were then used to generate inputs to a compartmental model of a layer 2 stellate cell (Figure S6 and [25]). Summation of aligned conjunctive cell inputs causes the postsynaptic neuron to have a grid firing field (Figure 4b). Crucially, when the activity of the co-aligned conjunctive cells was non-uniform across their different fields, the directional tuning of the postsynaptic cells across the whole environment was also non-uniform (Figure 4b) and individual firing fields were modulated by head direction (Figure 4c). These simulated firing patterns resembled the experimentally recorded directional tuning of grid cells (cf. Figure 4c with 2b). In contrast, when we simulated conjunctive cells with spatially uniform firing fields the firing fields of the downstream grid cells were not directionally modulated (Figure S7). The directional tuning of

individual firing fields in simulations with spatially non-uniform, but not spatially uniform, conjunctive cell inputs differed significantly from the corresponding shuffled data (Figure S8). Thus, integration of input from co-aligned non-uniform conjunctive cells can account for the local direction selectivity of grid cell firing.

Embedding of location-dependent directional information within grid cell firing fields has implications for the organisation of spatial and conceptual computations in entorhinal circuits and downstream structures. While more complex models that account for location-dependent directional firing of grid cells could be envisaged (Table S1), by showing how the firing fields of grid cells can result from integration of input from conjunctive cells [21,26], our results provide a parsimonious explanation that resolves discrepancies between functionally and anatomically defined cell types in MEC [27]. Entorhinal stellate cells, which are the major input to the hippocampal dentate gyrus and are required for spatial memory [28,29], appear to be the most numerous grid cell type, but less than half of stellate cells are grid cells [30]. This functional divergence is consistent with all stellate cells implementing similar cellular computations, but with the emergence of grid firing patterns depending on the identity of their dominant synaptic inputs. A key future question is how directional information encoded by grid cells is then used by downstream neurons. One possibility is that by disambiguating different views at the same location, directional firing by grid cells may facilitate pattern separation functions of the immediately downstream dentate gyrus [12–14]. Such view-dependent representations could also be a powerful computational feature of grid representations of visual and conceptual scenes [1,31,32].

5
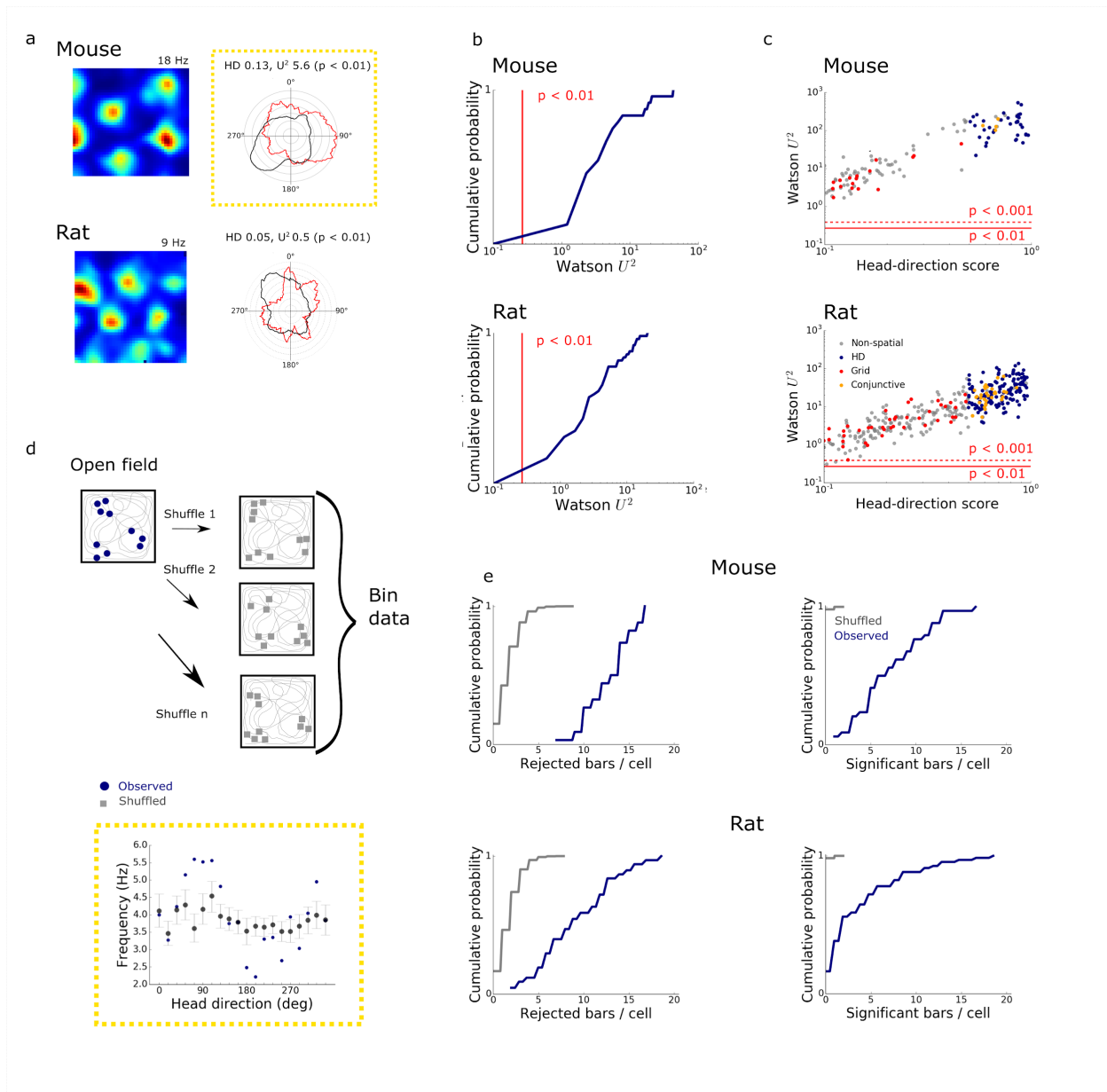
Figure 1. Grid cells firing is modulated by head direction. (a) Examples of firing rate maps (left) and head direction histograms (right) for grid cells from mice (upper) and rats (lower). Polar histograms show binned counts of head direction across all video frames (black) and the mean firing rate for each head direction bin (red). The head direction score (HD) and Watson U^2 test statistic for each cell are indicated above the polar plot. **(b)** Cumulative probability of the test statistic generated by a two-sample Watson U^2 test comparing the distribution of head directions when each cell fired to the distribution of head directions for the entire trajectory within the recording session (for mice: $p < 0.001$ for 34 out of 34 cells, for rats: $p < 0.01$ for 68 out of 68 cells). **(c)** Two sample Watson test statistics plotted as a function of head direction scores for grid cells (red), head direction cells (blue), conjunctive cells (orange) and other cells (grey). The red lines indicate significance levels $p < 0.001$ (dashed) and $p < 0.01$ (solid). **(d)** Schematic of shuffling analysis method (upper) and example of a directional firing rate

6

histogram for the mouse grid cell from (a) and its shuffled spikes (yellow box). Error bars indicate the 95 % confidence intervals. Circles represent recorded spikes, squares represent shuffled spikes. **(e)** The number of bars from each grid cell's directional histogram that are outside the 95 % confidence interval of the corresponding shuffled data (left) and the number of bars that differ significantly from the shuffled data ($p < 0.05$, two-tailed p value calculated from the shuffled distribution and corrected for multiple comparisons with the Benjamini-Hochberg procedure) (right). The distributions of the numbers of rejected bars and the distributions of number of significant bars per cell differed significantly between observed and shuffled data (n=34 grid cells from mice, n=68 grid cells from rats, for all comparisons $p < 10^{-16}$, Mann-Whitney U test).
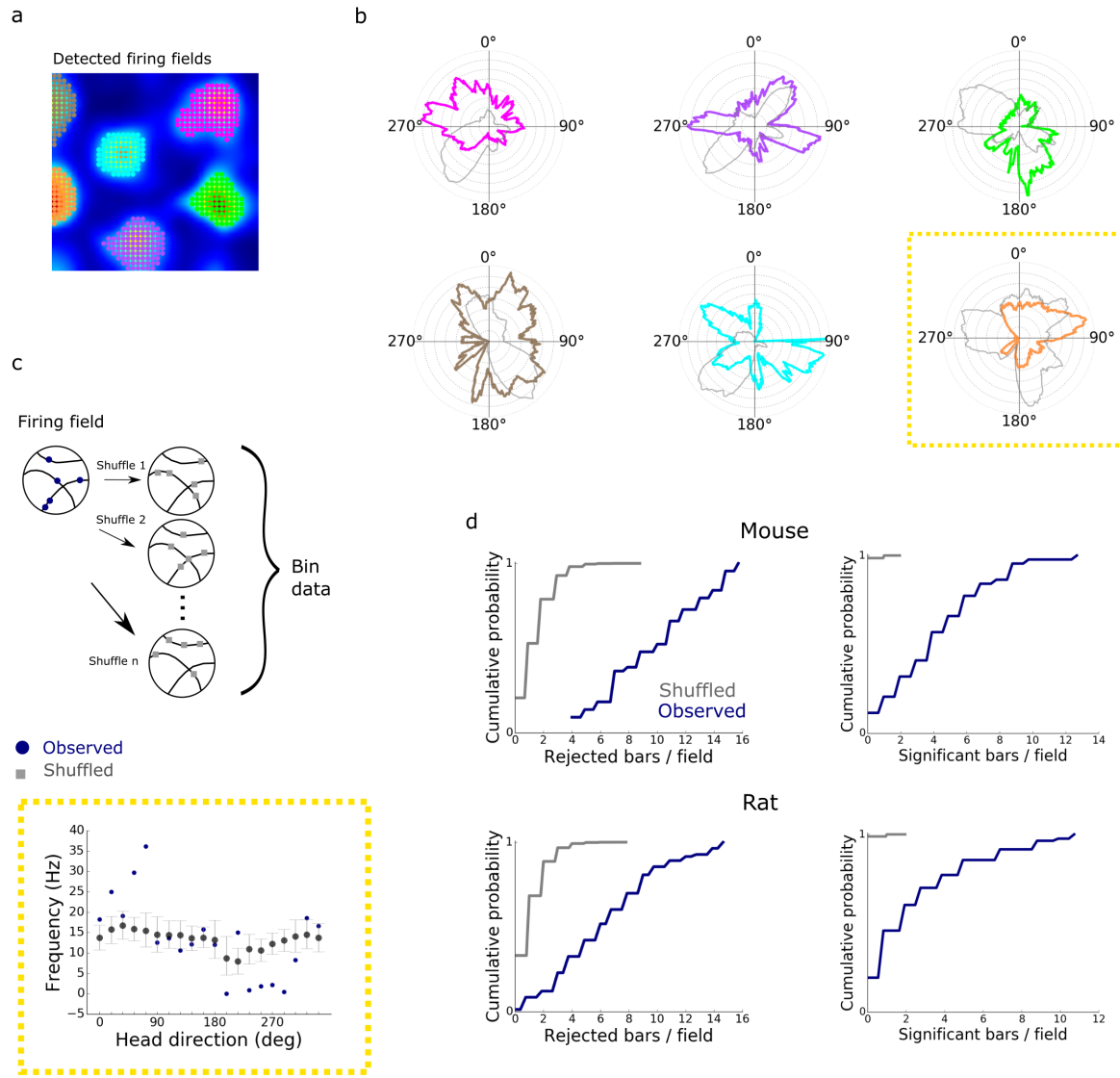
Figure 2. Individual firing fields encode head direction. (a) Firing rate map of the mouse grid cell from Figure 1a with colour-coded firing fields superimposed. **(b)** Polar head direction histograms for each firing field showing binned time spent by the animal with its head in each direction (grey) and mean firing rate for each bin (coloured according to (a)). Number of spikes from each field from left to right, top to bottom: 1455, 607, 646, 707, 628, 919. Amount of time spent in fields from left to right, top to bottom in seconds: 247, 102, 78, 136, 79, 83. **(c)** Schematic of shuffling method (upper) and example of directional firing rate histogram for observed and shuffled spikes for the highlighted field from (b, yellow boxes).The error bars represent the 95 % confidence interval of the shuffled distribution in each bar. **(d)** The total number of bars from each grid field's directional histogram that fall outside the 95 % confidence interval of its shuffled data (left) and the number of bars that differ significantly (threshold p < 0.05 after correction for multiple comparisons) from the shuffled data (right). The numbers of rejected bars and the number of significant bars differed between observed and shuffled data (n

8

= 44 fields from 13 grid cells, n = 83 fields from 25 grid cells, $p < 10^{-16}$ for all comparisons, Mann-Whitney U test).
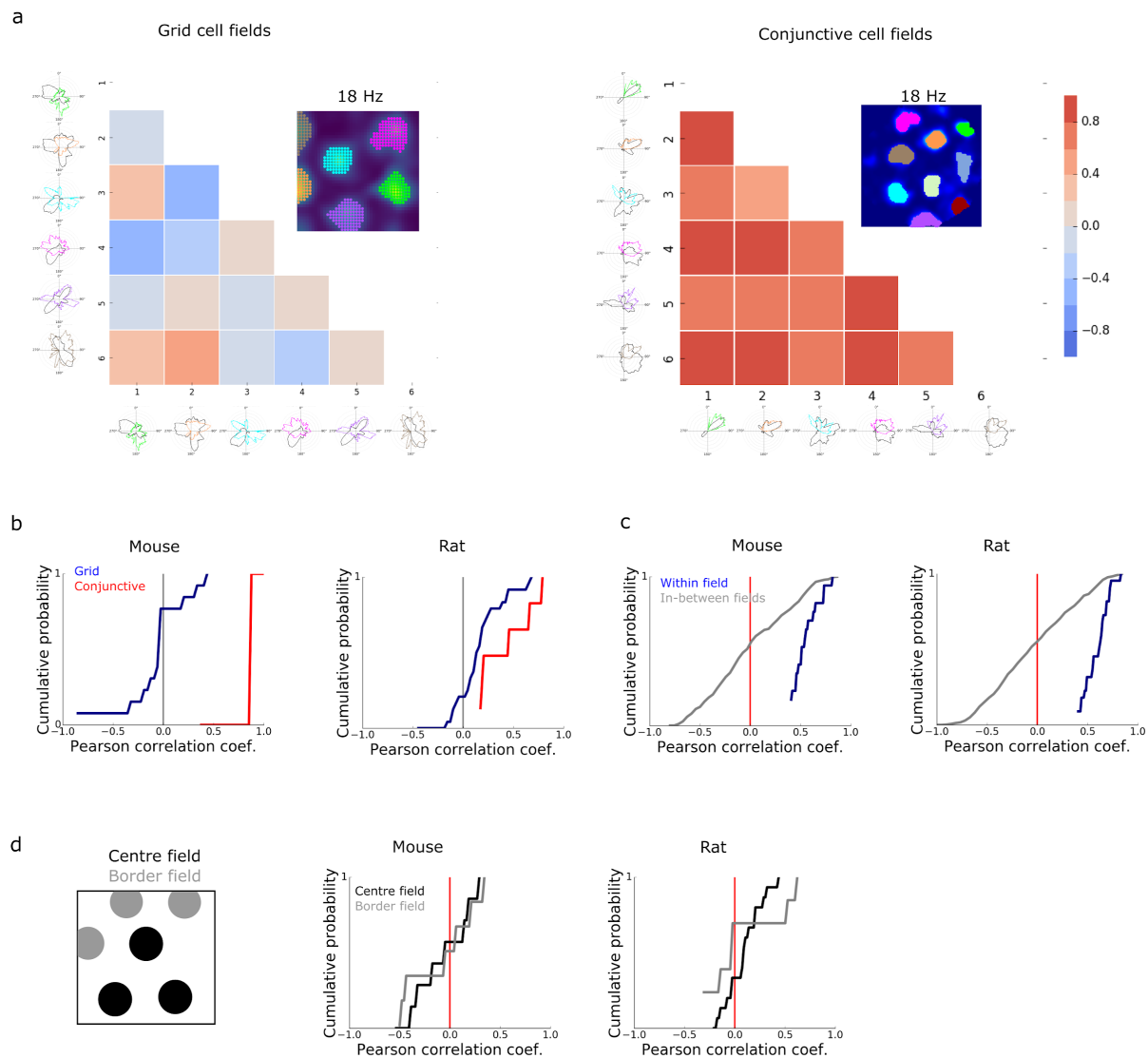
Figure 3. Directional firing by grid cells depends on location. (a) Example correlation matrices generated by pairwise correlation of binned head direction activity for firing fields from a grid cell (left) and a conjunctive grid cell (right). **(b)** The average Pearson correlation coefficient for grid (blue) and conjunctive (red) cells calculated as in (a). Each data point is the mean of the correlation coefficients from comparison of fields from one cell. **(c)** Correlations between firing rate histograms for the same field (blue) and between different fields (grey) generated from data from the first and second halves of the session. Only fields having within field Pearson R >= 0.4 were included in this analysis (correlations for all fields are shown in Figure S5). The within field and in-between field correlations differ significantly for mice and rats (p = 1.6 x 10^{-9} for n=18 fields from mice and p = 4.9 x 10^{-12} for n = 22 fields from rats, two-sample Kolmogorov-Smirnov test). Each data point is from correlation of one pair of fields. **(d)** Border and centre fields were defined based on whether they were contacted the border of the enclosure (left). Cumulative histograms show the distribution of between field correlation

coefficients calculated as in (b-c) but with central and border fields shown separately. Each data point is the mean of the correlation coefficients from comparison of fields from one cell.
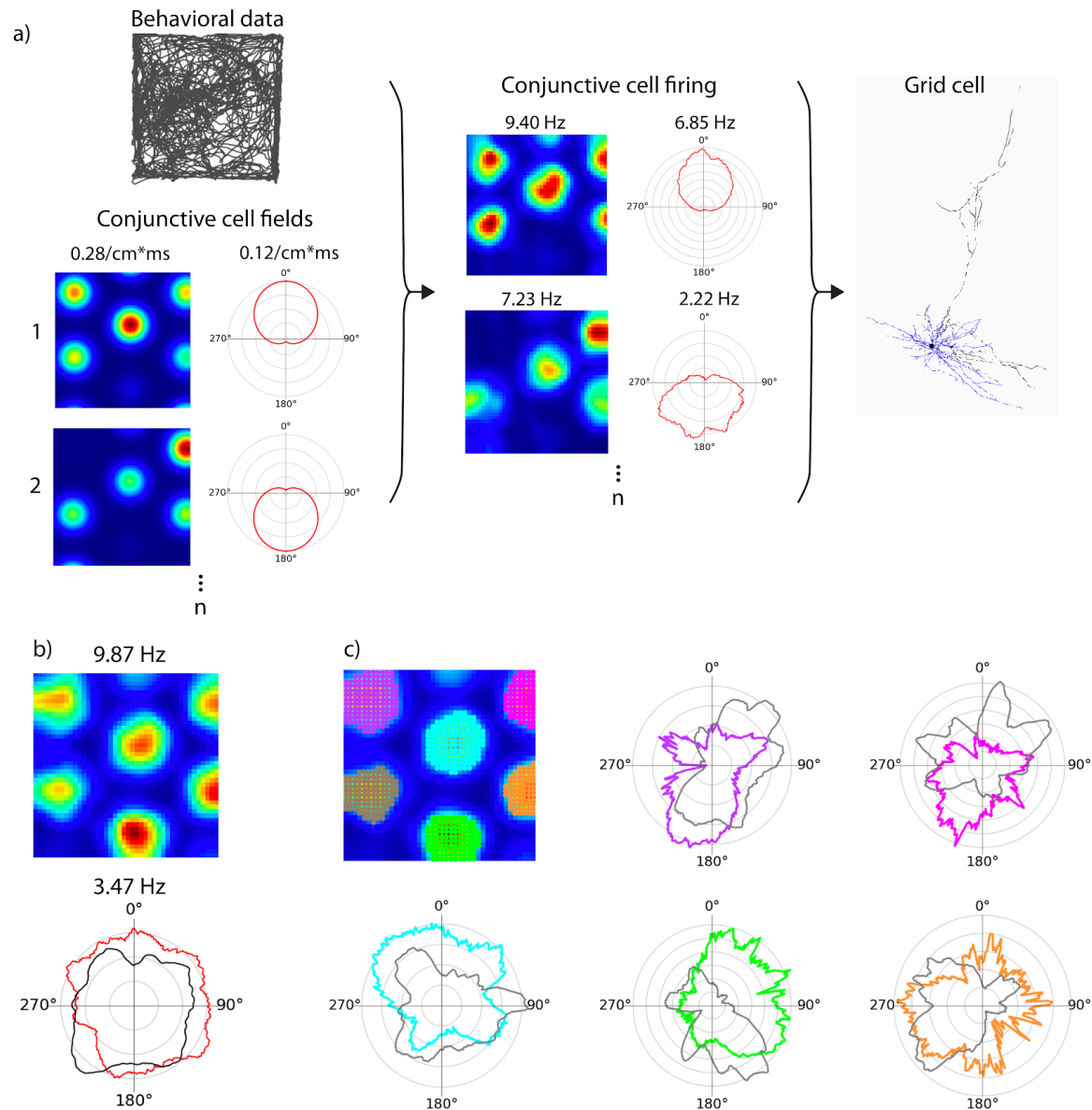
Figure 4. Direction-dependence of grid cell firing is accounted for by integration of co-aligned, non-uniform conjunctive cell inputs. (a) Rate map and head direction polar histograms of conjunctive cell firing probabilities (with the peak probability listed above) were convolved with the head direction and position of experimentally tracked mice to generate conjunctive cell firing fields (shown with peak firing rates). Firing times of the simulated conjunctive cells were used to trigger synaptic input to a compartmental model of a stellate cell. **(b)** Representative rate coded firing fields and head direction histograms from a simulation with 5 conjunctive cell inputs. **(c)** Head direction histograms for selected fields colour coded according the accompanying rate map.

Acknowledgements

Author contributions

KG and MFN conceptualised the study. KG performed experiments, developed code and performed analyses. JP developed and analysed simulations. KG, YP and MN contributed to statistical design. HS performed histology and imaging. MN obtained funding, supervised the project and wrote the manuscript. All authors contributed to review and editing of the manuscript.

Methods

Animals

All animal procedures were performed under a UK Home Office project license (PC198F2A0) in accordance with The University of Edinburgh Animal Welfare committee's guidelines. All procedures complied with the Animals (Scientific Procedures) Act, 1986, and were approved by the Named Veterinary Surgeon and local ethical review committee.

Sixteen p038 mice [33] (8 males and 8 females) 7-13 weeks (mean = 10.6, SD = 1.7 weeks) old at surgery were used. Before surgery animals were group housed (3-5 mice per cage) in a standard holding room on a standard 12 hour on/off light cycle (dark from 7 pm to 7 am). After surgery, mice were singly housed in a different holding room in otherwise similar conditions (average temperature 20°C, relative humidity 50%). Mice were kept in individually ventilated

cages containing sawdust, tissues, chewing sticks and cardboard tubes, which after surgery were replaced by a larger cardboard igloo. Two days after the surgery, a running wheel was placed in the cages. Standard laboratory chow and water were given *ad libitum*.

Microdrive design

We modified previous designs for 16-channel microdrives consisting of 4 tetrodes and an optic fiber [34,35]. We glued a 21 gauge 9 mm long inner cannula (Stainless Tube & Needle Co.LTD) to the hole next to the ground pin of an EIB-16 board (Neuralynx) using epoxy (RS components 132-605). Tetrodes were made with 18 μm HML-coated 90 % platinum 10 % iridium wire (Neuralynx). We connected two grounding wires (1.5 cm long insulated part) to the reference and ground pins of the EIB, threaded 4 tetrodes through the inner cannula and connected each tetrode wire to one of the pinholes of the EIB-16 board, fixing them with gold pins (Neuralynx, EIB Pins). A 13 mm long optic fibre stub (Plexon, PX.OPT-FS-Flat-200/230-13L) was threaded through the inner cannula, in between the tetrodes. We covered the wires on the board and the optic ferrule up to about 2/5th with epoxy and glued (RS components, 473-455) the tetrodes to four sides of the optic fibre. The next day we cemented a poor lady frame (Axona) to the side of the board. Finally, we put Vaseline around the base of the inner cannula, put the 17 gauge 7 mm long outer cannula (Stainless Tube & Needle Co.LTD) on the inner cannula.The tip of the outer cannula was sanded down diagonally so one side was 6 mm to fit the curvature of the skull. We trimmed the tetrodes using ceramic scissors (Fine Science Tools, Germany) to be 0.5 mm long from the tip of the optic fibre. The tips of the tetrodes were plated in a non-cyanide gold plating solution (Neuralynx). Tetrodes were cleaned, by applying three 1 second 4 μA pulses with the tetrodes as an anode and then plated by passing 2 μA 1 second pulses with the tetrodes as a cathode until their impedance was between 150 and 200 KΩ.

Microdrive implantation

We washed the tips of the tetrodes before the surgery with ethanol and then with sterile saline by holding them into a drop using a syringe. General surgical procedures and stereotaxic viral injections were carried out as described previously [24]. We induced inhalation anaesthesia using 5 % isoflurane / 95 % oxygen, and sustained at 1 – 2 % isoflurane / 98-99 % oxygen throughout the procedure (1 L / minute). Before implanting the drive, we injected AAV9-tre-ChR2-mCherry (Gene Therapy Center, University of Massachusetts Medical School)(800 -2000 nl total injection volume, 3-5 injections sites, 200 - 400 nl / site) for additional opto-tagging experiments (data not shown). All animals were injected 3.4 mm lateral relative to Bregma (Table S2). For electrical

14

grounding, we drilled two small craniotomies, and implanted M1 x 4 mm screws (AccuGroup SFE-M1-4-A2) on both sides about 3.4 mm lateral, and 1 mm rostral relative to Bregma.

To implant the microdrive we attached it to an Omnetics to Mill-Max adaptor (Axona, HSADPT-NN1) held by a crocodile clip attached to the stereotaxic frame. We lowered the tetrodes 1.5 mm into the brain, beginning 3.4 mm lateral from Bregma (right hemisphere of two mice, and left hemisphere of 14 mice) and targeting the dorsal third of the medial entorhinal cortex. We sealed the outer cannula with sterile Vaseline and fixed the implant by putting dental acrylic (Simplex Rapid powder) up to three quarters of the outer cannula, and around the foot of the frame, leaving the grounding screws uncovered. After the cement set, we carefully wrapped the grounding wires around the grounding screws (the reference wire was connected to the right side screw, and the ground wire to the left screw), and fixed the wires with silver paint (RS components 101-5621). After the silver paint dried, we applied another layer of dental acrylic to cover the skull and the grounding screws, but not the insulated part of the grounding wires, or the board, to ensure that the drive is able to move. We left mice to recover on a heat mat for approximately 20 minutes, moved them back to the holding room and gave them Vetergesic jelly (0.5 mg / kg of body weight buprenorphine in raspberry jelly) for 12 hours after surgery.

Open field exploration task

All recordings were performed in an open field arena consisting of a box made from a metal frame (parts from Kanya UK, C01-1, C20-10, A33-12, B49-75, B48-75, A39-31, ALU3), with removable metal walls, a polarizing cue on one wall, and a floor area of 1 m^2. A camera (Logitech B525, 1280 x 720 pixels Webcam, RS components 795-0876) was mounted on the top of the frame for motion tracking. To record head direction we used a custom Bonsai script [36] to track red and green polystyrene balls attached to either side of the mouse's head.

Mice were handled three times a week for 5 - 10 minutes for four weeks following surgery. For 3 consecutive days before recording we habituated the mice by allowing them to explore the open field arena for 5 -10 minutes. For recording sessions, mice explored the open field arena unrewarded until they covered the whole area, or for a maximum of 90 minutes. An opto-tagging experiment was performed at the end of each session (data not shown). After each recording session we lowered the tetrodes by 50 μm using the drive mechanism on the implant.

For electrophysiological recording, the 16 channel optetrode was connected to an Open Ephys acquisition board [37] and computer (HP Z440 Tower Workstation i7, 16GB, 512GB SSD, Cat.: J9CO7EA#ABU) using an SPI cable (Intan Technologies, RHD2000 6-ft (1.8 m) Ultra Thin SPI interface cable C3216) and via a commutator (SPI cable adapter board, Intan Technologies C3430 and custom 3D printed holder). Signals were filtered between 2.5 Hz - 7603.8 Hz using a second order Butterworth filter implemented in Open Ephys. We aligned position and electrophysiology data using light pulses generated at random intervals (20 s to 60 s) by an LED (light-emitting diode) attached to the side of the open field arena hidden from the mouse but in the field of view of the camera. An Arduino script controlled delivery of pulses to the LED and the Open Ephys acquisition board.

Post recording assessment of tetrode locations

To enable determination of tetrode locations, after the last recording day we applied a 2 second ~20 µA current to burn the tissue at the tip of the electrodes. We then anesthetized the mice using isoflurane and pentobarbital, intracardially perfused PBS (phosphate buffered saline, Gibco, 70011044, 10 times diluted with distilled water) for 2 minutes, then 4 % PFA (paraformaldehyde, Sigma Aldrich, 30525-89-4) in 0.1 M PB (phosphate buffer, Sigma Aldrich, P7994) for 4 minutes at a 10 mL / minute flow rate. We left the brains in 4 % PFA in 0.1 M PB for 16 hours, then transferred them to 30 % sucrose (Sigma Aldrich, S0389) in PBS until they sank.

We cut 50 µm sagittal sections of the fixed brains using a freezing microtome. Sections were processed to label them with primary antibody rat anti-mCherry (Invitrogen M11217, 1:1000) followed by secondary antibody goat anti-rat alexa 555 (Invitrogen A-21434,1:1000) and stained with either NeuroTrace 640/660 (Invitrogen N21483, 1:500) or NeuroTrace 435/455 (Invitrogen N21479, 1:500) following procedures described previously [24]. Images were taken on a Zeiss Axio Scan Z1 using a 10x objective and visually inspected to determine the final position of the recording electrodes (see Extended Data). We classified recording sites to be in the deep MEC, superficial MEC, parasubiculum or not possible to determine.

Data analyses

Analyses were carried out using Python (version 3.5.1 in Anaconda environment 4.0) and R version: 3.3.1 (2016-06-21). All code will be available at https://github.com/MattNolanLab.

Spike sorting

To isolate spikes from electrophysiological data we used an automated analysis and clustering pipeline based around MountainSort (v 0.11.5 and dependencies)[38]. Python scripts pre-processed the data by converting Open Ephys files to mda format and organized these files together with spike sorting input parameter files. We defined the four channels of each tetrode to be in the same 'sorting neighbourhood'. We excluded broken channels identified during data acquisition from the geometry files.

MountainSort filtered the data from 600 Hz - 6000 Hz using a bandpass filter and then performed spatial whitening over all 16 channels to remove correlated noise. Events with peaks three standard deviations above average and at least 0.33 ms away from other events on the same channel were detected. The first 10 principal components of the detected waveforms were calculated, creating a 10-dimensional feature space. A spike sorting algorithm, ISO SPLIT, was applied on the feature space [38]. The algorithm first over-clusters the data, and then performs pair-wise checks on clusters to ensure that the two main assumptions are met, and regroups spikes if necessary.

Cluster quality was evaluated using metrics for isolation, noise-overlap, and peak signal to noise ratio [38]. Units that had a firing rate higher than 0.5 Hz, isolation more than 0.9, noise overlap less than 0.05, and peak signal to noise ratio more than 1 were accepted for further analysis. Any units that did not have a refractory period or hyperpolarization component of their spike waveform were discarded. These exclusions were based on visually assessing output figures generated for sorted clusters. No additional manual curation was done to modify the assignment of individual firing events to clusters.

Classification of functional cell types

To classify recorded neurons we used established grid and head direction scores [3]. Grid scores were defined as the difference between the minimum correlation coefficient for rate map autocorrelogram rotations of 60 and 120 degrees and the maximum correlation coefficient for autocorrelogram rotations of 30, 90 and 150 degrees [39]. The firing rate map was calculated by summing the number of spikes in each location and dividing that by the time the animal spent there and then smoothing the surface with a Gaussian centred on each location bin ([12]). Autocorrelograms were calculated by shifting the binned firing rate map [12] into every possible

17

binned position along both horizontal and vertical axes and calculating correlation scores for each of these positions. This rate map was converted into a binary array using a 20 % threshold on normalized data. If the binary array had more than 7 local maxima, a grid score was calculated. Subsequent parts of the analysis, where correlations between the rotated autocorrelograms were calculated, only included the ring containing 6 local maxima closest to the centre of the binary array, excluding the maximum at the centre. The ring was detected based on the average distance of the 6 fields near the centre of the autocorrelogram (middle border = 1.25* average distance, outer border = 0.25 * average distance).

To calculate head direction scores, the head direction angles corresponding to the firing events of each neuron were first binned into 360 bins between 0 and 2π. The obtained polar histogram was smoothed by calculating a rolling sum over a 23 degree window. For angles between -179 and 180 degrees in steps of 1 degree, dx and dy were calculated in a unit circle (radius = 1), as $dy = \frac{sin(angle)}{radius}$ and $dx = \frac{cos(angle)}{radius}$. To obtain the x and y components of the head direction vector, the head direction polar histogram was multiplied by the dx and dy values, respectively, and normalized to the number of observations in the polar head direction histogram, so that $x_{total} = \frac{\Sigma(dx \cdot HD_{histogram})}{\Sigma HD_{histogram}}$ and $y_{total} = \frac{\Sigma(dy \cdot HD_{histogram})}{\Sigma HD_{histogram}}$. The head direction score was then calculated using the Pythagorean theorem as head direction score=

$$\sqrt{(x_{total}^2 + y_{total}2)}\quad.$$

We defined grid cells as cells with a grid score ≥ 0.4, which was chosen as a conservative threshold (cf. [22]). We defined head direction cells as cells with a head direction score ≥ 0.5. We defined conjunctive grid cells as cells that passed both head direction and grid cell criteria.

Identification and analysis of individual fields

We identified individual firing fields using methods similar to those used previously to detect place fields [40]. The open field arena was divided into 42 x 42 bins, where each bin contained a smoothed firing rate value calculated by summing the number of spikes at the locations corresponding to each bin, dividing this by the time the animal spent in the bin and then smoothing the surface with a Gaussian ($e^{\frac{-x2}{2}}$) centred on each bin [12]. We next identified the

bin of the rate map with the highest firing rate. If the rate was higher than the average firing rate plus the standard deviation of the rest of the rate map, we added bins with adjacent sides that had a firing rate higher than 35 % of the local field maximum to the field. We recursively added to the field further bins that satisfied these criteria with respect to the newly added bins. We accepted a detected field if it had more than 45 bins, but it was smaller than half of the arena. After successfully detecting a field, it was removed from the rate map by replacing the values with zeros and the analysis was repeated until we found no more fields. All detected fields were visually assessed and if a detected field appeared to be a combination of two fields or only part of a field, it was tagged as a false positive to be excluded from the analyses.

Analysis of head direction

Two-sample Watson test. To evaluate whether head direction when the cell fired differed from the head direction of the animal during the time spent in a field, or arena, we performed Watson's two sample test [41,42] for homogeneity on the two distributions using R package circular.

Bootstrap tests. Shuffled head direction locations were generated by random selection with replacement of locations from the trajectory of the animal, either inside the whole environment or in a given field. The randomization was weighted with the firing rate of the bin where the spike happened to rule out that directional firing is a result of different sampling of directions in different bins of the rate map [19]. The number of selected random locations was equal to the number of times the neuron fired in the environment or field.

Analyses compared the observed data with 1000 shuffled data sets. The range of possible head directions was segmented into 18 degree bins. For each shuffled data set, the head direction associated with each randomized event was binned. To obtain a simulated firing rate, the total number of spikes for each bin was normalized to the amount of time the animal spent facing the range of directions associated with the bin. Two analyses were carried out. First, for each 18 degree interval, the bins where the observed frequency was outside the 95% confidence interval of the randomized data were counted. Second, for each bin the percentile position of the observed data relative to the randomized data was used to calculate a p value. The twenty p values within a field were corrected for multiple comparisons using the Benjamini-Hochberg procedure and the number of intervals where the corrected p values were < 0.05 were counted. To obtain null distributions the same analyses were performed for each of the 1000 randomized

19

data sets, where each shuffle was treated like the observed data and was compared to the distributions from the 1000 shuffles.

Correlation between directional firing histograms. Pearson correlation coefficients were calculated (scipy.stats.pearsonr) for pairs of histograms of head direction dependent firing rates. Histograms used in these analyses were generated by dividing the histogram of heading directions when the cell fired by the histogram of head directions from the trajectory to obtain a firing rate (Hz) for each angle. The histograms were smoothed using a 23 degree rolling window. Bins with 0 Hz firing rates were excluded from the correlation analyses.

Rat data

Data from rats [3] was downloaded from the Kavli Institute's online database (https://www.ntnu.edu/kavli/research/grid-cell-data). The data was available in a format that contained the trajectory of the animal and firing times of sorted cells in MATLAB files. The MATLABfiles were converted into a spatial data frame similar to the mouse data so the same analysis scripts could be used to perform all analyses.

Stellate cell model

All simulations were performed in the NEURON simulation environment [43]. Simulation code will be available at https://github.com/MattNolanLab.

The model stellate cell used a previous morphological reconstruction of a mouse MEC layer 2 stellate cell [25]. Voltage-gated sodium and potassium channels were inserted into the soma and axons (channel models from [44]), HCN channels were inserted into the dendrites and soma (channel models from (Schmidt-Hieber and Häusser, 2013)) and leak channels were inserted into all compartments. Maximum channel conductances were adjusted so that electrophysiological properties of the neuron were similar to the experimentally determined properties of stellate cells [45], with the resting membrane potential (RMP), input resistance, sag, rheobase spike peak and half-width fit within the range of experimental values [46]. The best fit for voltage threshold that could be achieved was within 30% of the mean experimentally determined values. RMP was defined as the average membrane potential over 4 s with no current input. Spike peak and half-width were determined from a single suprathreshold

20

response to a 20 ms depolarizing current, where peak potential was the maximum voltage and half-width was the width of the spike at a voltage halfway between RMP and the peak. Sag ratio was determined in response to a 40 pA hyperpolarizing current step and defined as the ratio between the peak decrease and steady state decrease in voltage. Voltage threshold was defined as the highest voltage reached without spiking and was determined from responses to a series of 3 s duration current steps with progressively increasing amplitude. Rheobase was defined as the current required to initiate a spike and was determined using a current ramp increasing linearly from 0 - 150 pA over 2 s. Input resistance was determined as the slope of the line fitted to the voltage increase resulting from current injections between 0.0016 nA to 0.048 nA.

The modeled cell received simulated synaptic input from conjunctive cells. Synapses were randomly localized to dendritic locations with 9 synapses per input cell. The probability of synapse placement on a dendrite was given by the ratio of the dendrite length to the total basal or apical dendritic length. Synapses generated fast conductance changes with an instantaneous rise and exponential decay of 2 ms (cf. [25]). All synapses had the same maximal conductance, which was determined for each number of conjunctive cell inputs simulated (Nc). To do so we measured the model response to Nc inputs activated at 12 Hz across a range of maximal conductances. The conductance that achieved a maximal postsynaptic firing rate of 12 Hz was selected by fitting the responses as a function of conductance with a second order polynomial.

Simulation of conjunctive cell firing

To simulate firing of conjunctive cells we first generated for each cell a grid pattern and a head direction tuning curve. For the grid pattern, the centre of each field was specified from the vertices of equilateral triangles with a length of 50 cm that were aligned to tessellate the simulated environment. Each cell had the same spatial phase. Each firing field was described by a circular Gaussian distribution with a full width at half maximum (FWHM) of 20.0 cm. To generate non-uniform field maxima (cf. [22]), the peak for each field was scaled by a random value from a uniform distribution between 0 and 1. The grids were then scaled to have a peak height of 1. The head direction tuning curve consisted of a Gaussian centered around a preferred direction with a FWHM of 141 degrees and a height of 1. The preferred head direction was dependent on the total number of inputs to the downstream grid cell, such that the preferred head directions were evenly distributed between 0 and 360 degrees. For each simulated conjunctive cell, firing probability distributions were calculated from the grid pattern

21

and a head direction tuning curve at a spatial resolution of 1 cm. The probability of firing was determined by multiplying the individual probabilities of the grid and head direction components by a factor of 0.28 and 0.12 respectively. These values were chosen to generate peak spatial firing rates around 12 Hz and peak head direction firing rates around 5 Hz, which are comparable to experimental data [3].

Conjunctive cell spike times were generated for a behavioural trajectory within a 1 x 1 m open field. The x and y position was determined every ms and if the probability of each cell firing was greater than a random number between 0 and 1 the cell spiked. For 100 simulated conjunctive cells, the peak spatial firing rate was 12.3 ± 2.71 Hz and the normalized peak head direction firing rate was 4.94 ± 1.04 Hz.

Each conjunctive cell was connected at 9 synapses to the downstream stellate cell. To evaluate representations generated in the stellate neuron model, we simulated 20 trials for each Nc. Each trial differed in the randomly determined synapse placement of each conjunctive input and in the randomly determined peaks of the conjunctive cell fields.

Supplementary Figures

a

b
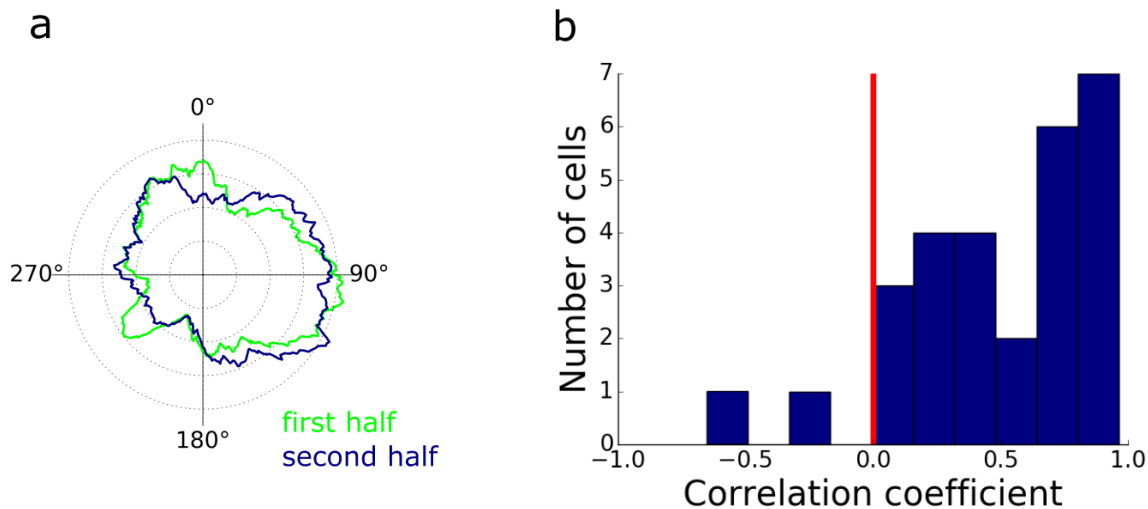
Figure S1. Head direction preferences of grid cells in the first and second half of the session are stable in recording sessions in mice. (a) Polar histograms of normalized head direction from the first (green) and second half (blue) of the recording session for the grid cell shown on Figure 1a. **(b)** Histogram of Pearson correlation coefficients (mean = 0.47, SD = 0.39) between head direction histograms from the first and second halves of the recording sessions for grid cells.
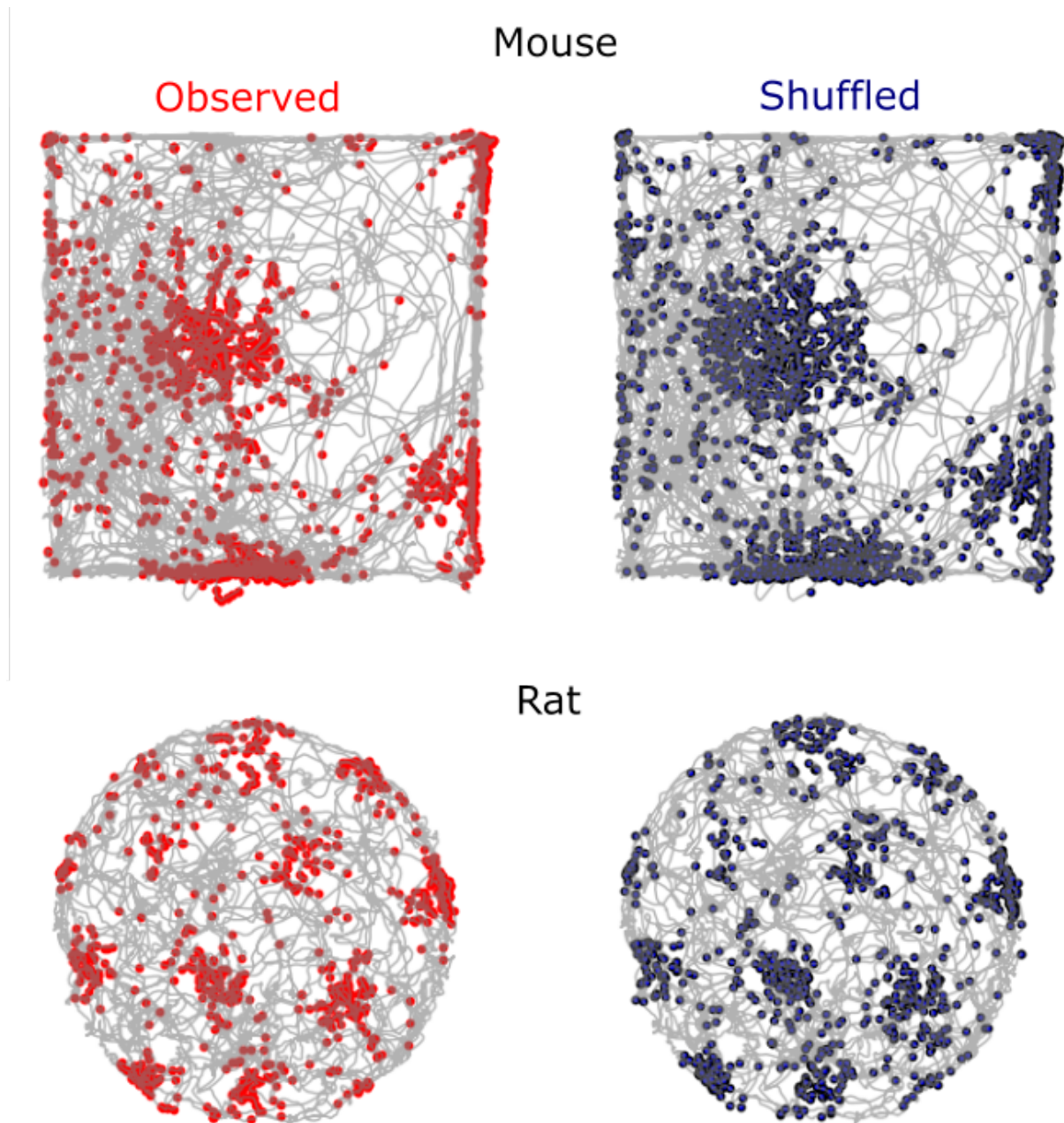
Figure S2. Shuffling maintains the location-dependent firing rate. Examples of observed (left) and shuffled (right) spikes from a mouse (top) and a rat (bottom). Grey lines are the trajectories of the animal.
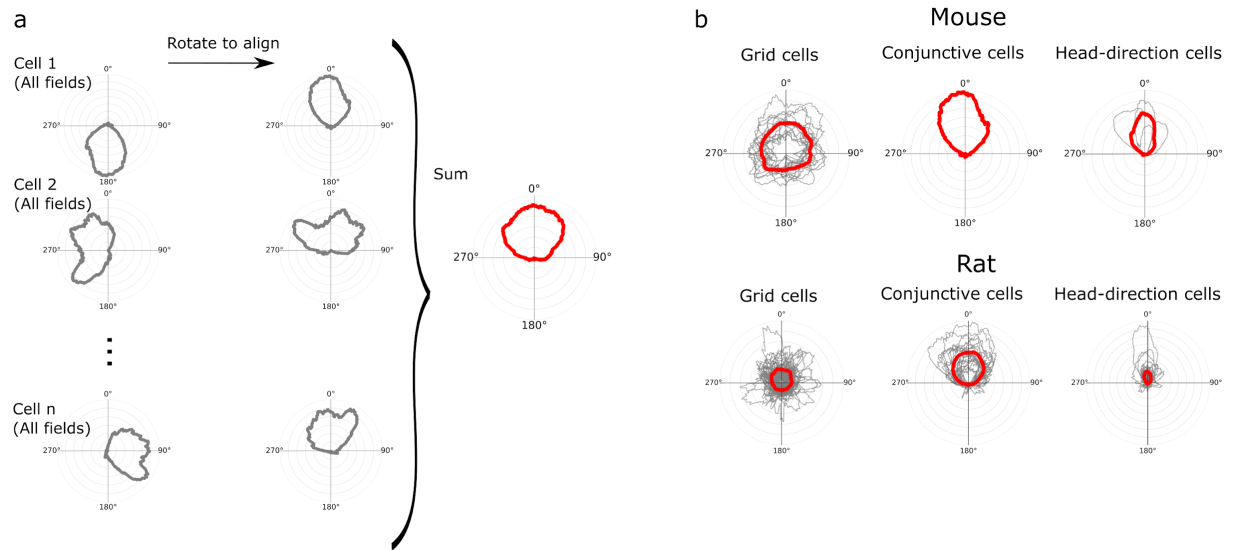
Figure S3. (a) Schematic of procedure for evaluating similarity of directional firing fields. Polar histograms of head direction dependent firing rates of data from all detected fields were rotated by the population mean vector of the combined distributions of head direction in all detected fields of a given cell to align them at 0. The examples shown here are for conjunctive cells. **(b)** Overlaid polar head direction histograms of grid cells, conjunctive cells and head direction cells with firing fields. Mean histograms are in red. In the histograms for grid cells the directionality appears smoothed by averaging indicating that there is no consistent shape to the firing field, whereas for head direction and conjunctive cells the averaged field appears unimodal.
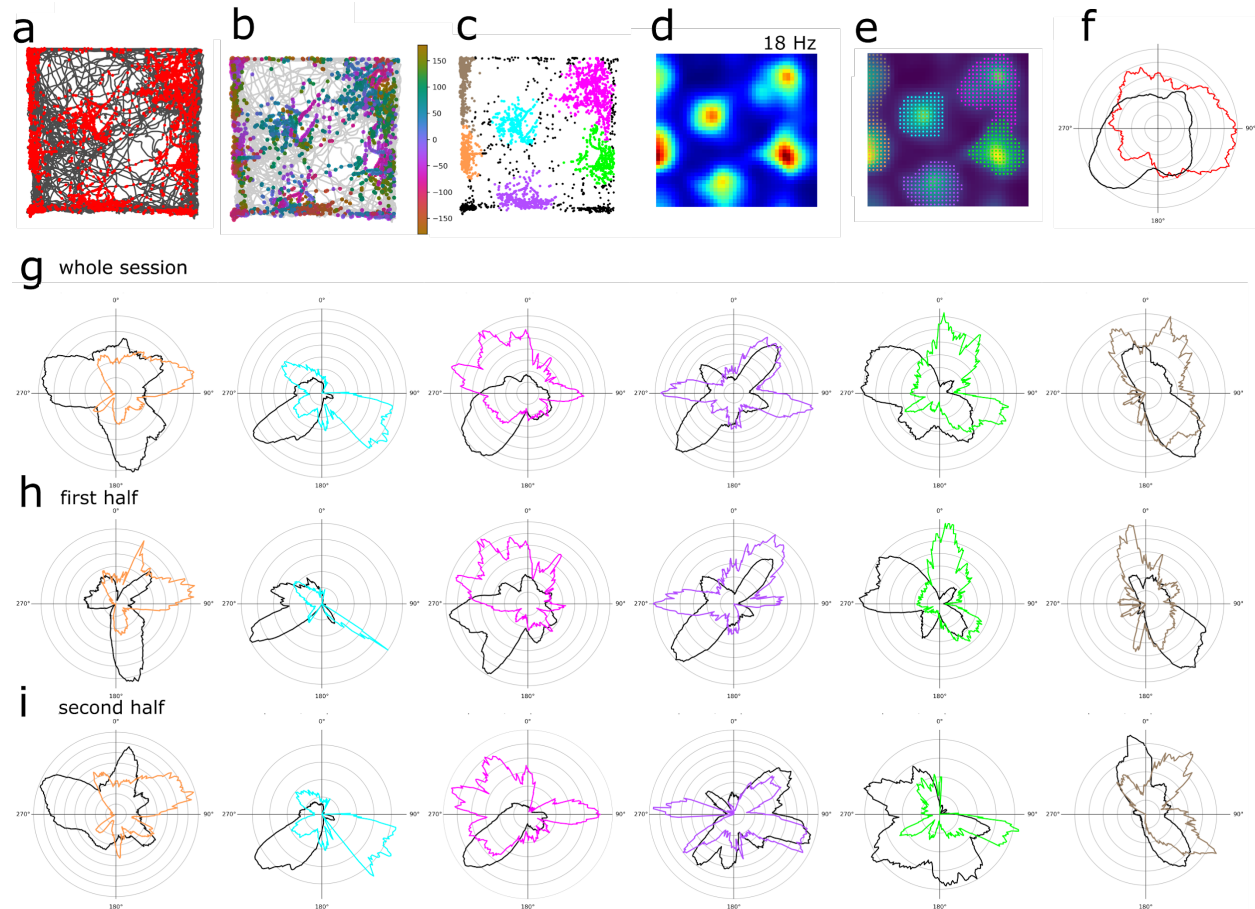
Figure S4. Head direction preferences recorded in mice are stable between the first and second half of recording sessions. (a-i) Data for an example grid cell. **(a)** Spikes (red dots) on the trajectory (black line) from the whole session. **(b)** Spikes colour coded for head direction. **(c)** Spikes colour coded for grid field identity (black dots are not included in any fields). **(d)** The firing rate map. **(e)** Detected firing fields marked on the rate map with coloured dots. **(f)** Polar head direction histograms were generated by plotting a smoothed (10 degree window) polar histogram of the animal's head direction from the whole session (black, normalized value) and when the cell fired (red, in Hz) normalized to the time spent in the field. **(g)** Polar head direction plots generated from data extracted from firing fields during the whole session. Number of spikes and time spent in fields from left to right: 919, 628, 1455, 607, 646, 707 spikes, and 83, 79, 247, 102, 78, 136 seconds. **(h)** Polar plots of head direction of fields during the first half of the recording. Number of spikes and time spent in fields from left to right: 353, 144, 683, 350, 405, and 395 spikes, and 36, 15, 126, 71, 41, 74 seconds. **(i)** Polar plots of head direction of fields during the second half of the session. Number of spikes and time spent in fields from left to right: 566, 484, 772, 257, 241, and 312 spikes, and 47, 64, 121, 31, 36, 62 seconds. Pearson correlation coefficients were calculated for the field histograms from the first and second half of the recording. Correlation coefficients for pairs of fields from (h) and (i) from left to right are 0.82, 0.34, 0.38, -0.02, -0.09, 0.35. p values for fields 4 and 5 were 0.09 and 0.7, respectively, and < 0.0001 for all other fields for the correlation.

26
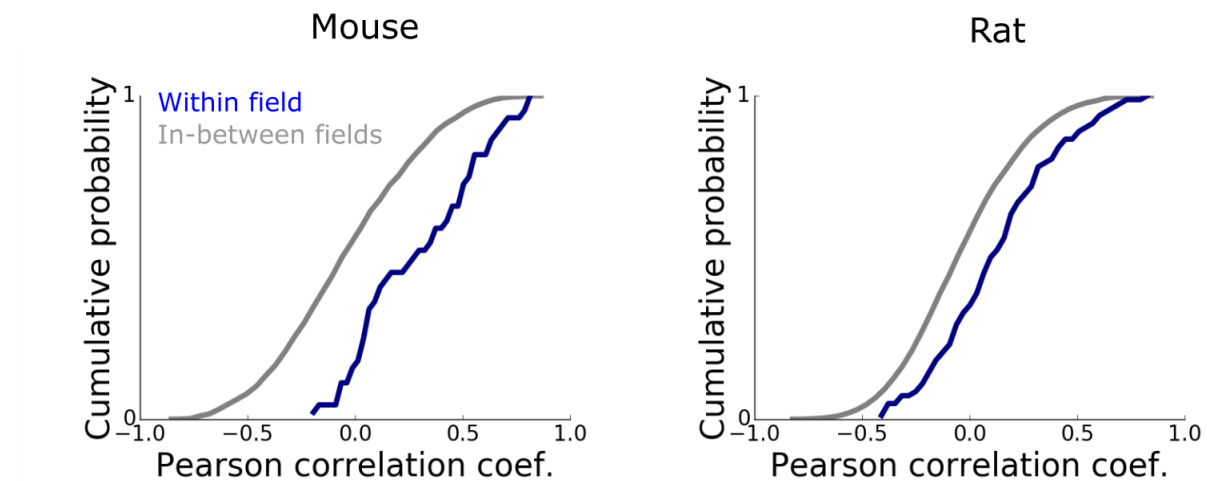
Figure S5. Correlations between firing rate histograms generated from data from the first and second halves of each recording session. Plots show the distributions of correlation scores between the same field (blue), and between different fields (grey). The within field and in-between field correlations differ for mice and rats (two-sample Kolmogorov-Smirnov test, p = 1×10^{-4} for mice and p = 1×10^{-4} for rats). All fields were included in this analysis. The result is consistent with Figure 3 in which only fields with high correlation between the first and second halves of the recording are included.
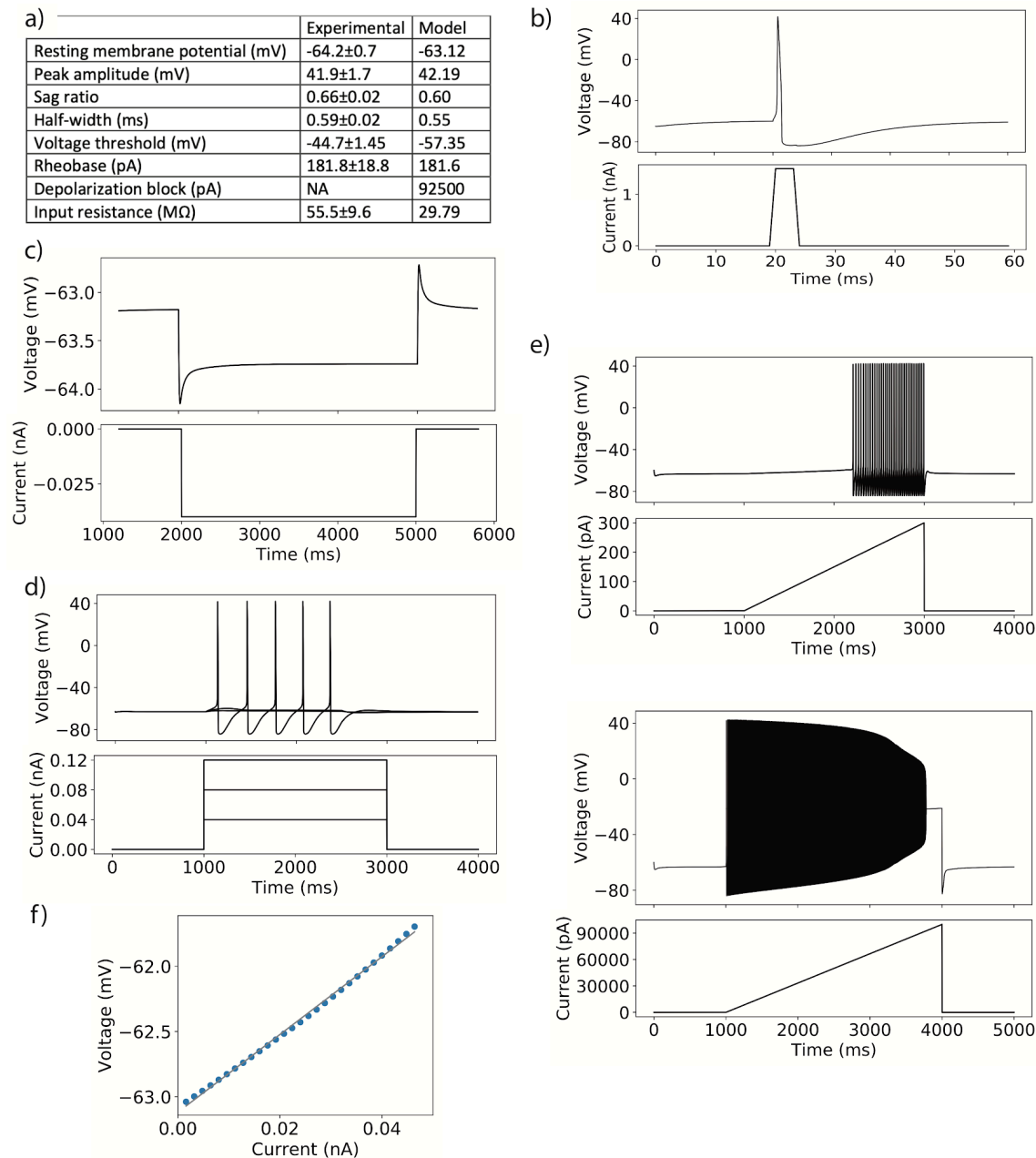
Figure S6. Characterization of grid cell model. (a) Summary of electrophysiological properties of the model compared to experimental data [46]. **(b)** Single action potential used to determine peak-amplitude and half-width (upper) and injected current (lower). **(c)** Voltage response to injection of a 40 pA hyperpolarizing current used to determine the sag ratio. **(d)** Voltage responses (upper) to increasing current steps (lower) used to determine voltage threshold. **(e)** Voltage responses (upper panels in each pair) to injection of ramp currents (lower panels in each pair) to determine the rheobase and depolarization block. **(f)** Determination of input resistance as the slope of the linear fit of steady-state voltage change induced by small current injections.
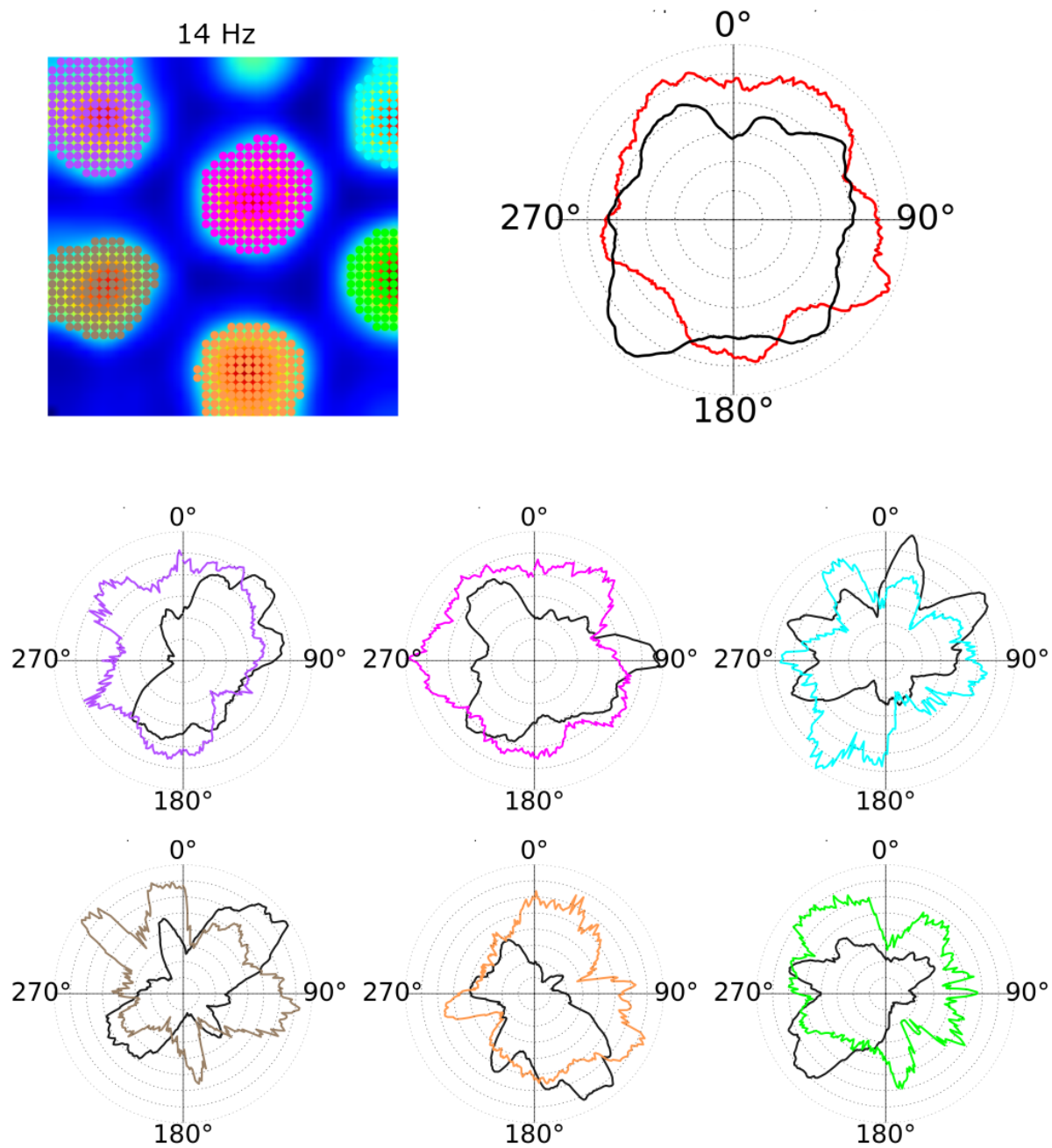
Figure S7. Firing fields of simulated grid cells receiving input from conjunctive cells with uniform firing rates in their field do not demonstrate directional firing. Example firing rate map and head direction tuning resulting in grid cell from convergence of 5 aligned and uniform conjunctive cells. Selected grid fields indicated in the rate map, and their individual grid field head direction tuning is plotted with grid field occupancy (grey).
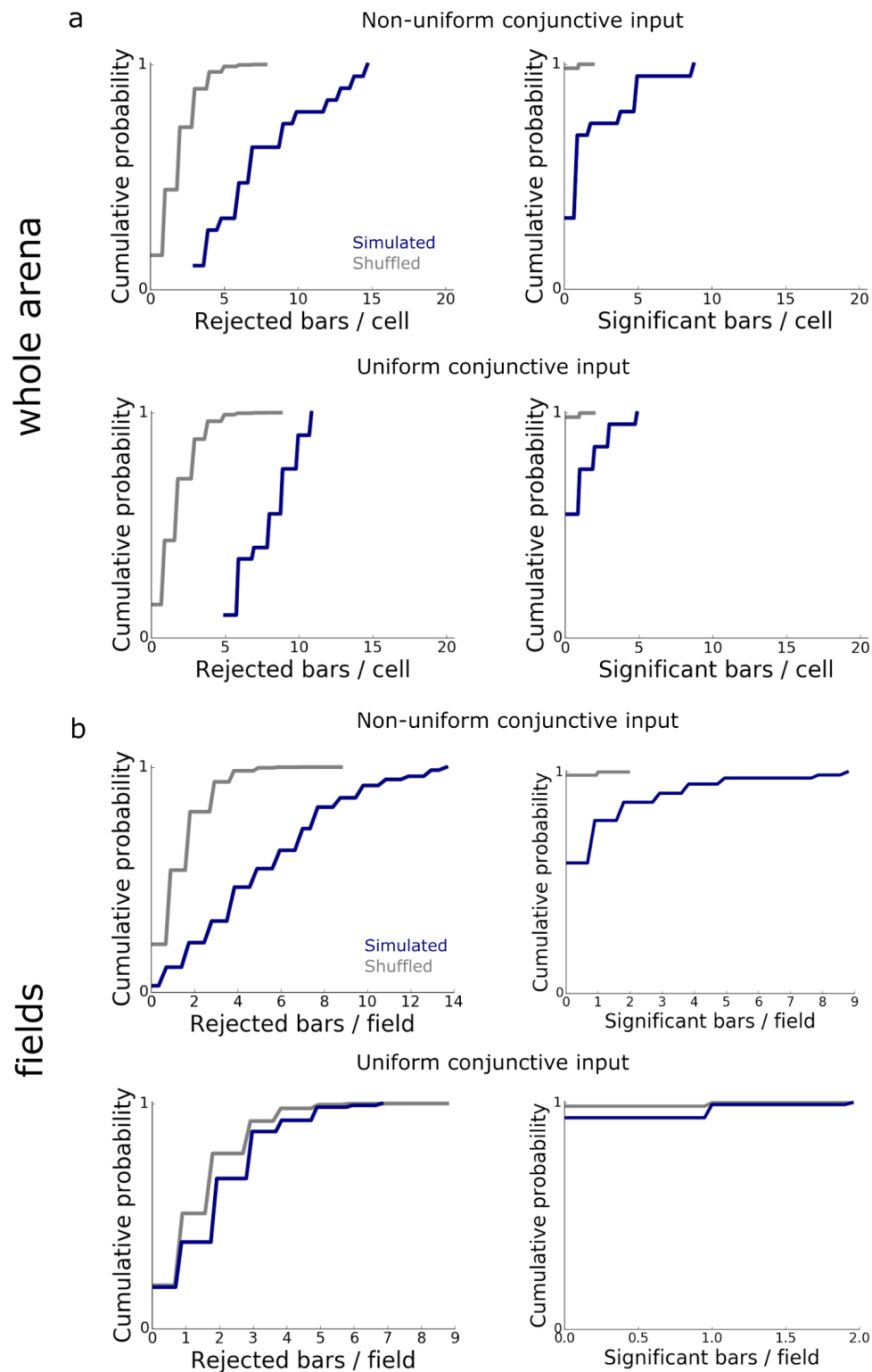
Figure S8. Grid cells that receive input from conjunctive cells with uniform firing rates in their field do not have directional firing.

(a) Results of simulations of stellate cells receiving input from five conjunctive cells and analysed as in Figure 1d-e. Upper plots are for simulations with non-uniform conjunctive cell input (cf. Figure 4b) and lower plots are for simulations with uniform conjunctive cell inputs (cf. Figure S7). Cumulative histograms show the number of bars from each simulated sellate cell's directional histogram (n=20 simulated grid cells) that are outside the 95 % confidence interval of the corresponding shuffled data (left) and the number of bars that differ significantly (p < 0.05, two-tailed p value calculated from the shuffled distribution and corrected for multiple comparisons with the Benjamini-Hochberg procedure) from the shuffled data (right). The distributions of the numbers of rejected bars from the shuffled and observed data were significantly different for cells (top) that received input from 5 conjunctive cells with variable firing rate maxima in their firing fields (p = 3.7×10^{-7}, Mann-Whitney U test) ,and also for grid cells (bottom) that received input from 5 conjunctive cells with uniform firing rates (p = 0.0007, Mann-Whitney U test).

(b) Results of a similar analysis to (a) performed on the individual firing fields of the simulated cells (cf. 2c-d and Figure 4c). Cells receiving non-uniform conjunctive input (top) had directional firing that significantly differed from shuffled data (p = 3.4×10^{-9}, Mann-Whitney U test). The directional firing of grid cells that received uniform input (bottom) did not differ from the shuffled data (p = 0.3, Mann-Whitney U test).

Model	Predicted head direction modulation	References	Notes
Continuous attractor network models	Unidirectional or uniform omnidirectional	4,5,8,10	1
Oscillatory interference models	Uniform omnidirectional	9,47	2
Synaptic plasticity models	Uniform omnidirectional	48,49	3
Integration of sub-threshold grid fields and location-dependent head direction fields	Localised head direction modulation of grid firing	No previous publications	4
Integration of conjunctive cell inputs	Localised head direction modulation of grid firing	Figure 4 and Figures S6-8	5

Table S1. Comparison of predictions for directional modulation of grid cell firing made by grid models. References are to example publications and are not exhaustive. Notes for each model:

1. Continuous attractor network models assume that grids result from activity bumps driven around a recurrent network by inputs that encode speed and head direction. Depending on their configuration the models predict either unidirectional head direction modulation (e.g. [50]) or spatially uniform omnidirectional modulation (e.g. [8]). Models with unidirectional head direction firing can account for the properties of conjunctive cells. Because spatially uniform directional modulation is a requirement for these models to generate grid fields they are unlikely to explain the local head direction modulation reported here.

2. Oscillatory interference models generate grid fields through summation (or multiplication) of multiple oscillatory inputs that are tuned to a particular direction and have phase modulated by running speed. Because the effect of direction on firing rate is very weak in these models and as uniform directional modulation of input phase is a requirement for these models to generate grid fields they are unlikely to explain the local head direction modulation reported here.

3. In plasticity models grid fields emerge through synaptic plasticity mechanisms in conjunction with adaptation rules (e.g. [48]) or training signals (e.g. [51]). To date grid cells generated through these mechanisms appear to have omnidirectional firing fields with no local modulation of directional tuning (cf. [51]).

4. It is conceivable that grid cell firing patterns are generated through a purely sub-threshold mechanism. In other words grid patterns are generated by membrane potential changes that alone are insufficient to trigger action potentials. In this scenario, additional input from head direction cells with local spatial firing fields, would convert the silent cell into a grid cell with

local-directionally modulated firing fields. A challenge for this scenario is to establish biophysical mechanisms that would ensure that alone neither the grid pattern generator or the head direction input will drive action potential firing.

5. The scenario we proposed here assumes that co-aligned conjunctive cells make convergent synaptic input onto the common postsynaptic neurons. We show here that these postsynaptic neurons will have grid firing fields that are locally modulated by head direction. This model contrasts with the previous scenario (4) which requires multiple relatively complex and untested assumptions.

animal ID	implanted depth (mm)	final location (mm)	distance travelled (mm)	estimated angle	recording site
A	1.6	2.15	0.55	90	**deep**
B	1.8	2.3	0.5	100	not in MEC
C	1.4	2	0.6	90	not in MEC
D	1.6	2.3	0.7	100	parasubiculum
E	1.5	2	0.5	90	parasubiculum
F	1.6	2.3	0.7	100	**superficial**
G	1.5	2.3	0.8	90	**deep**
H	1.5	1.7	0.2	110	**superficial**
I	1.5	2.3	0.8	100	**superficial**
J	1.5	2.3	0.8	90	not in MEC
K	1.5	2.3	0.8	90	**deep**
L	1.5	2.15	0.65	90	**superficial**
M	1.5	2.2	0.7	90	**superficial**
N	1.5	2	0.5	80	**deep**

Table S2. Estimated position of tips of recording electrodes at the beginning and end of experiments and estimated recording sites in deep and superficial layers of the MEC. Estimated angles are relative to the straightened skull and are based on histology images. Two animals were terminated for health reasons and their brains were not processed.

Extended data

1. Area of tetrode recording location for each experimental animal from in vivo open field experiments. 50 um sagittal sections were stained with NeuroTrace and expression of AAV-TRE-ChR2-mCherry was enhanced with anti-mCherry. Sections were imaged at 10x objective by Zeiss Axio Scan Z1. Scale bar is 500 μm.
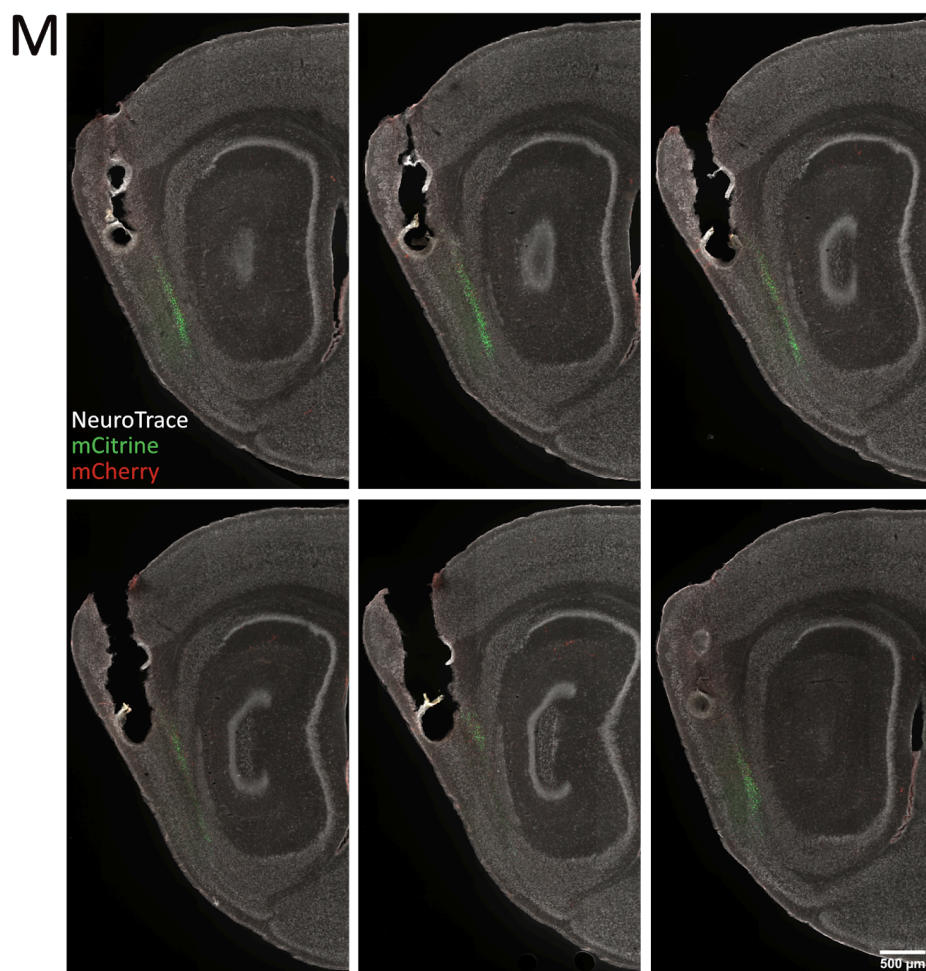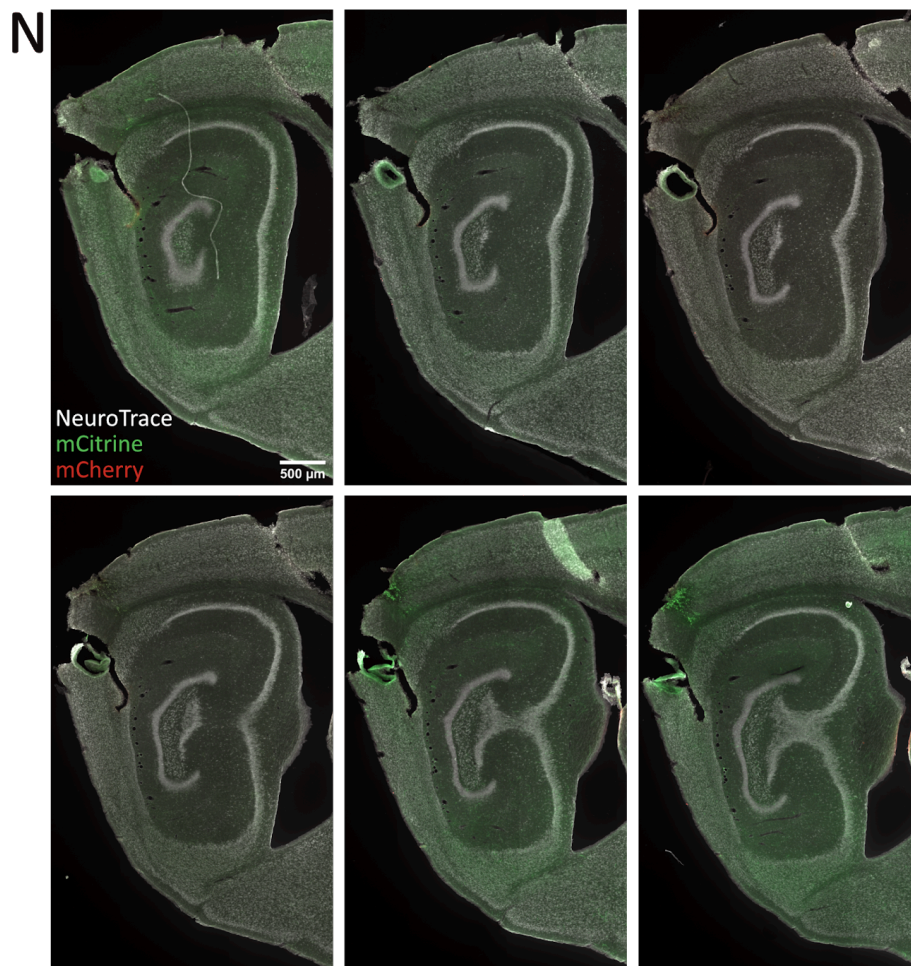
38
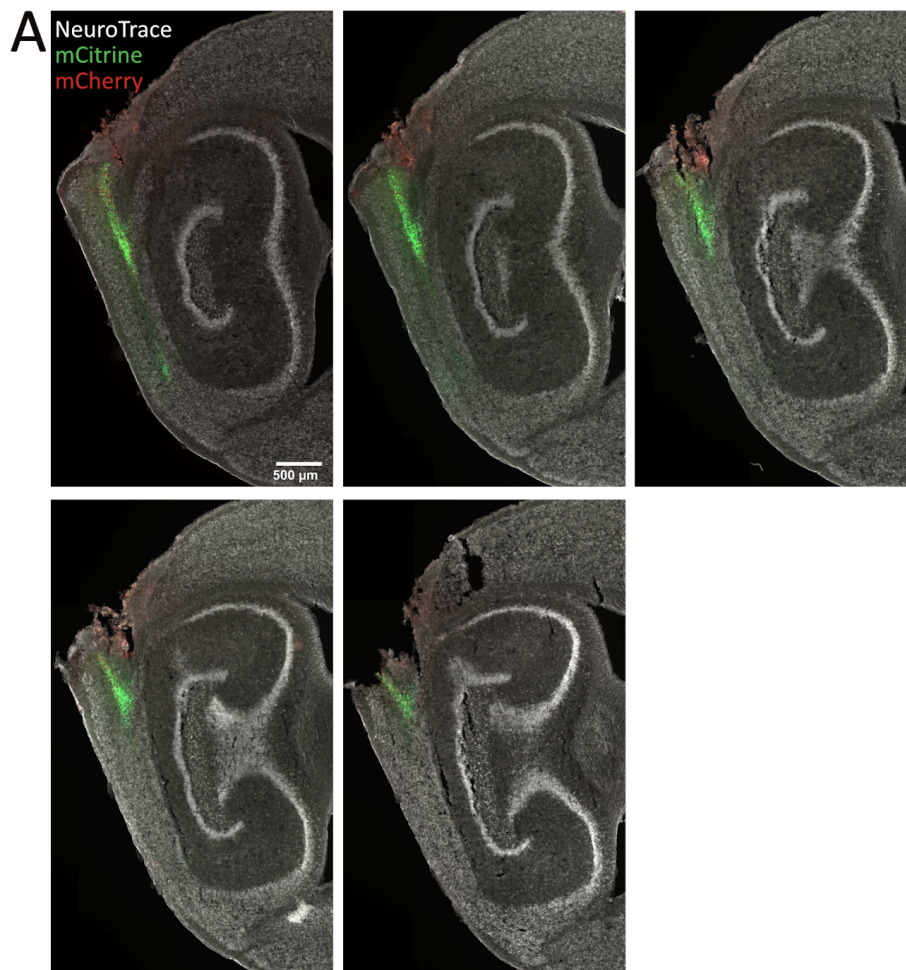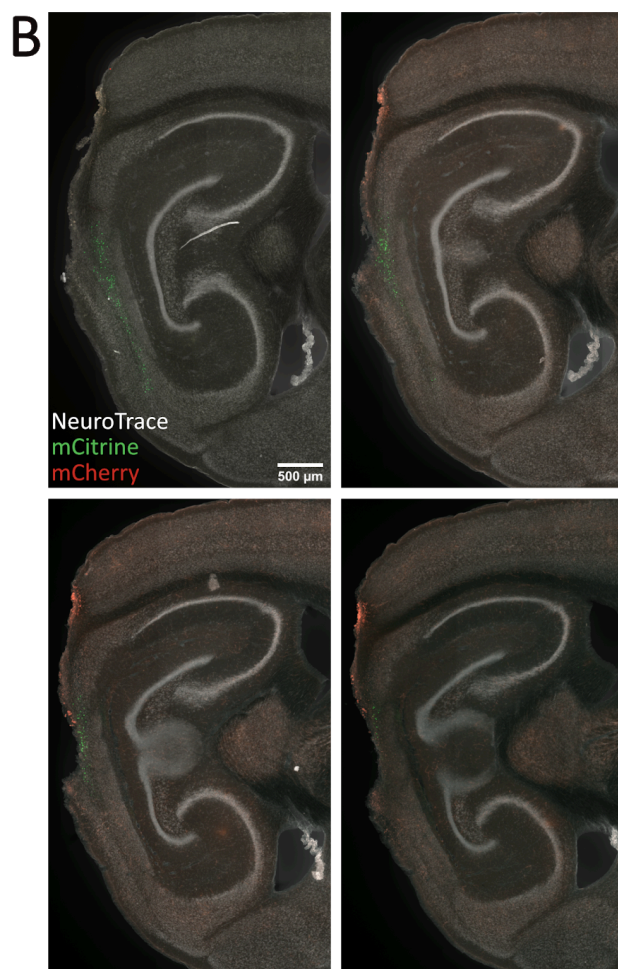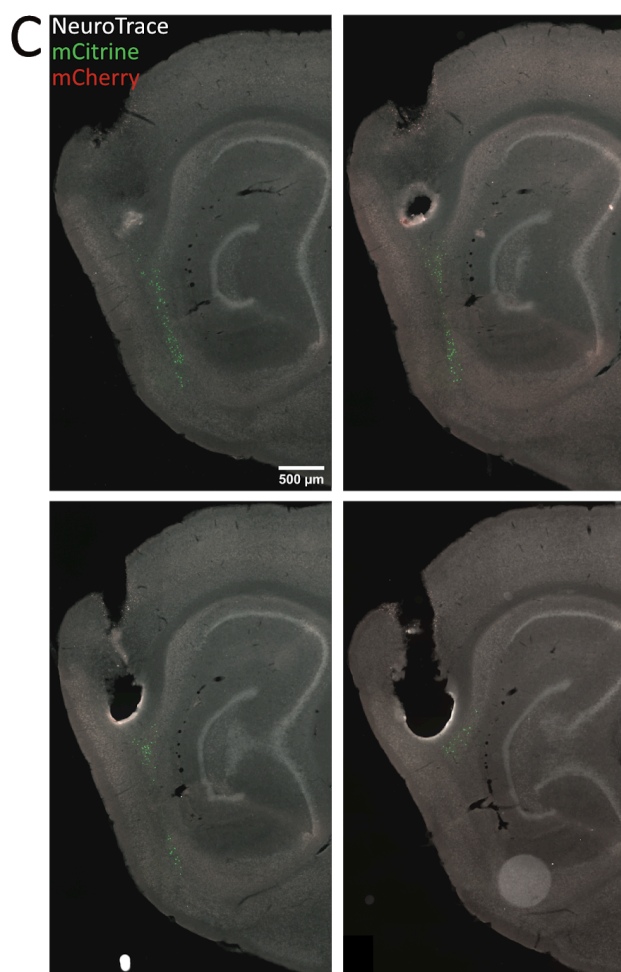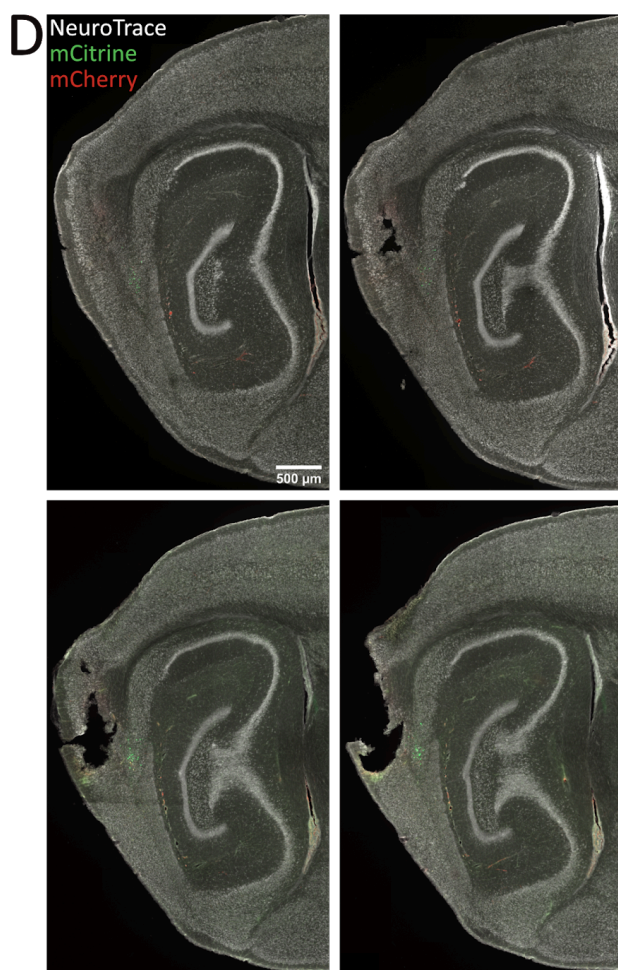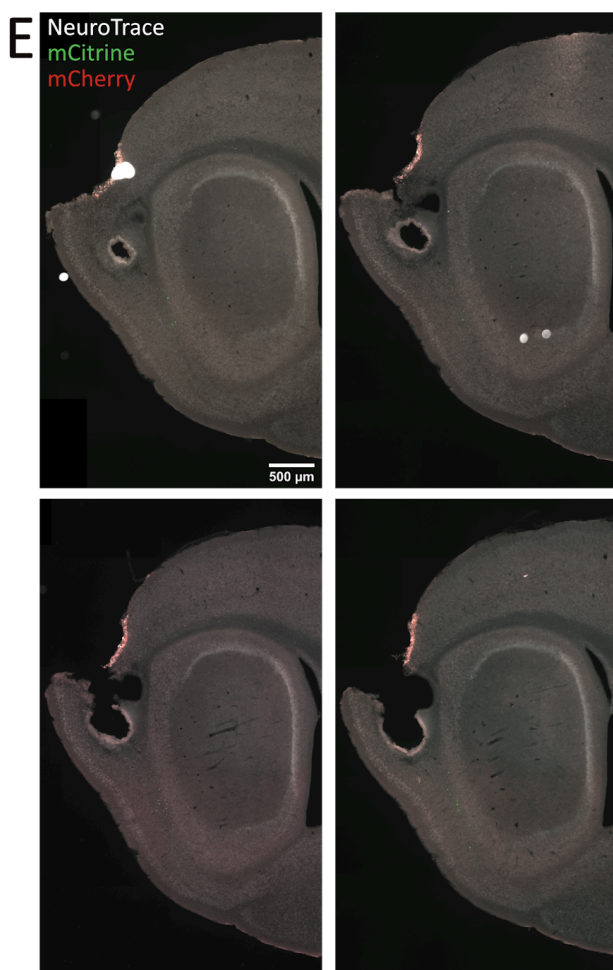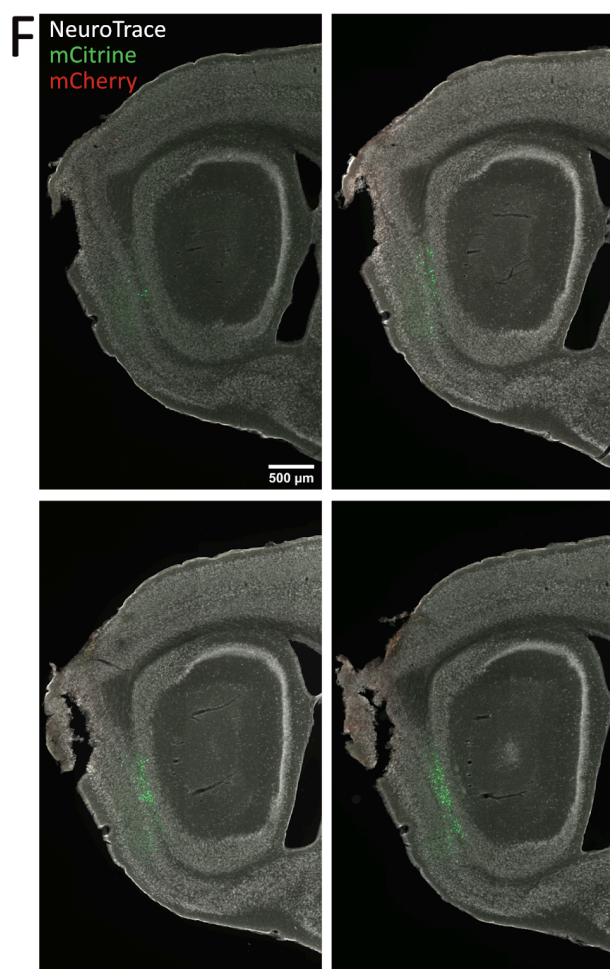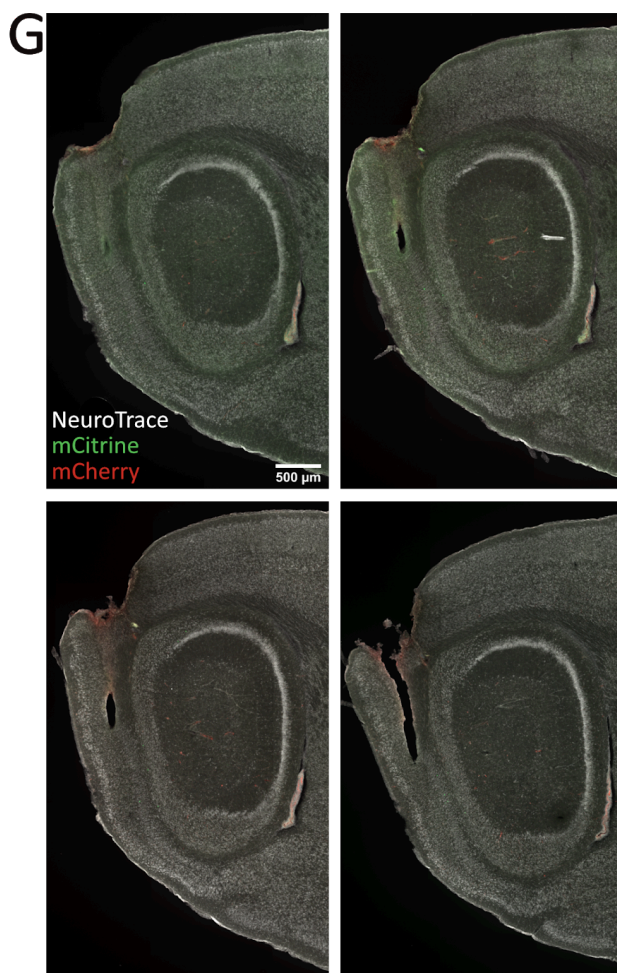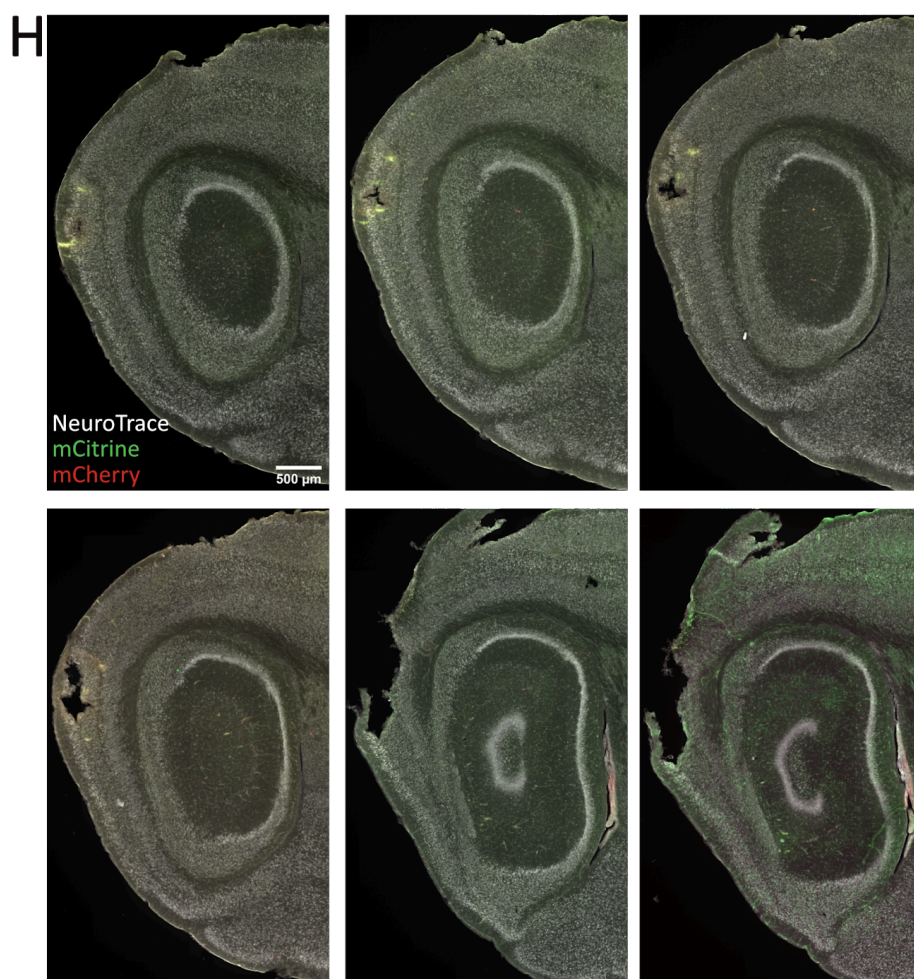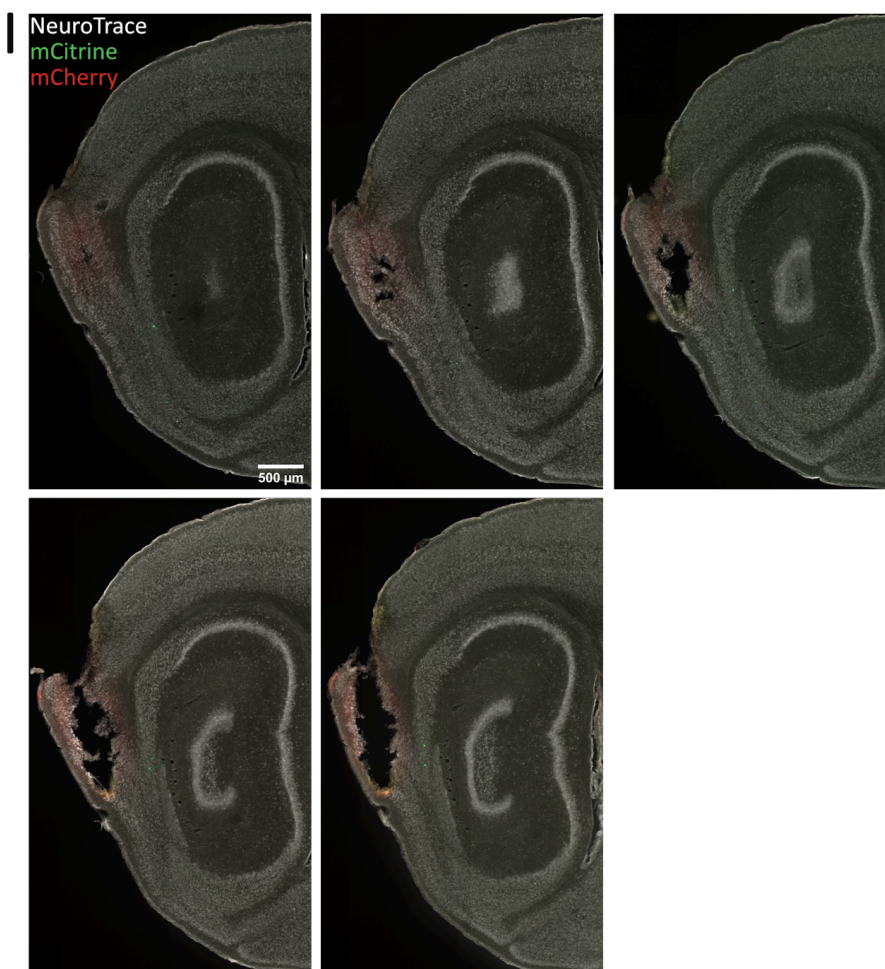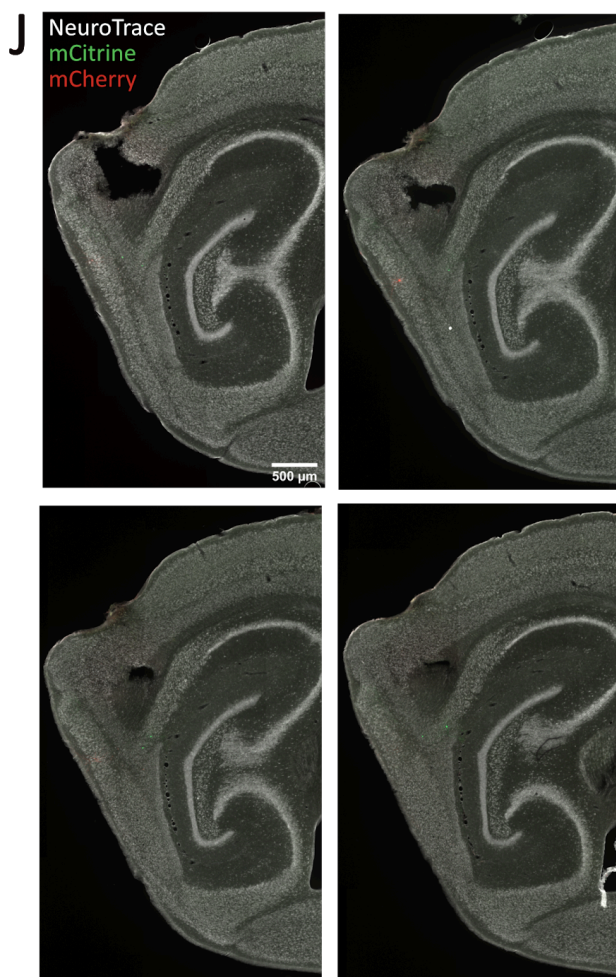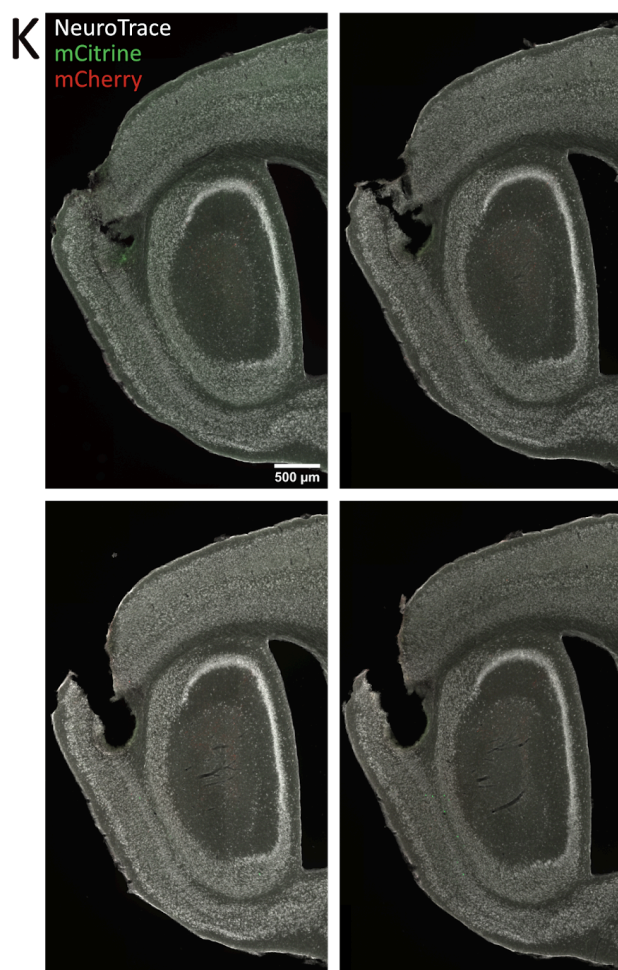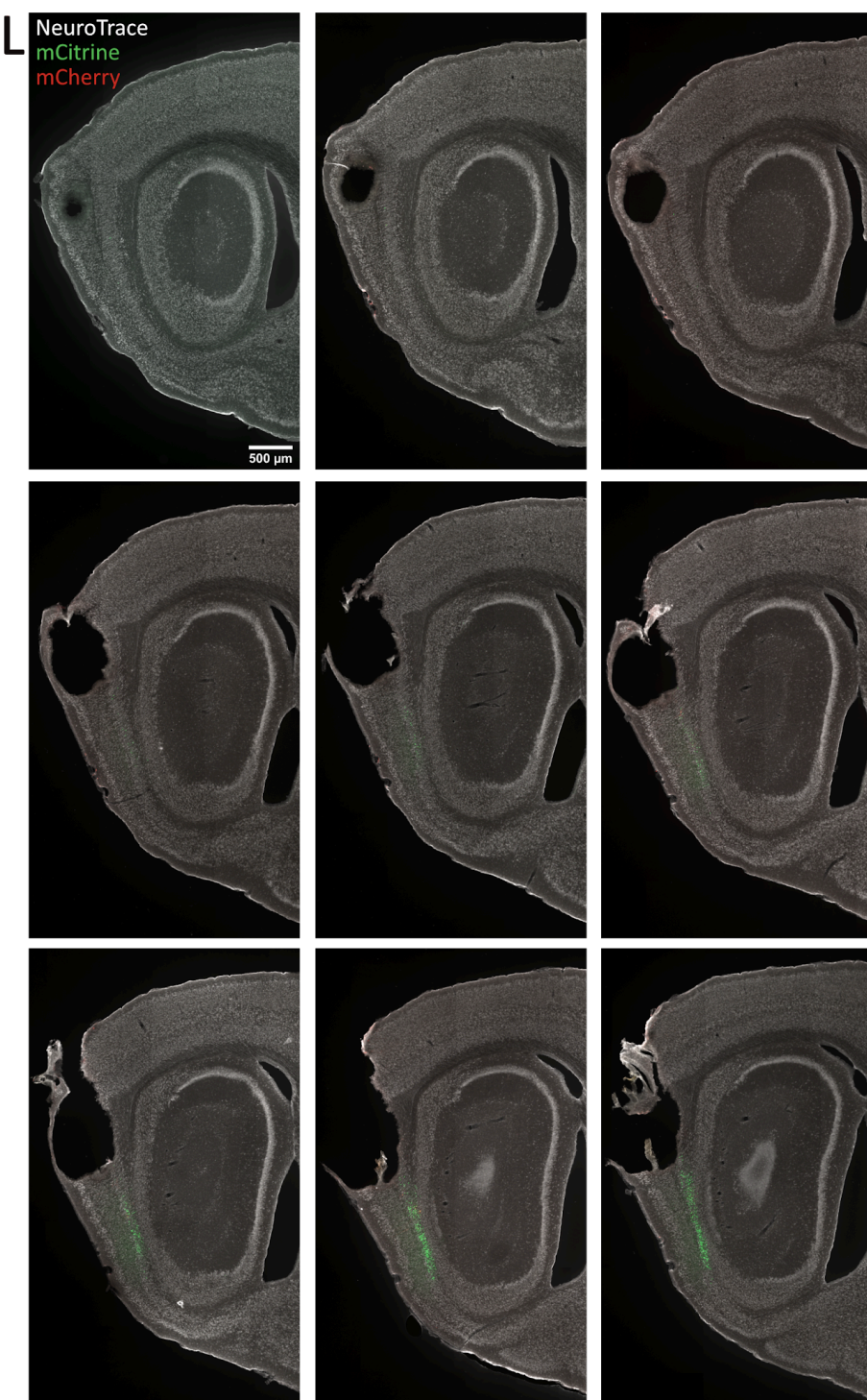
2. Mouse grid cells with more than two successfully detected firing fields. Each series of plots summarises data from a single grid cell. Top row left to right: action potential waveforms overlaid for the four channels of the tetrode, autocorrelograms of spike times, histogram of firing times over time, histogram of speed during firing events. Second row left to right: trajectory of the animal (black line) and firing events (red dots), firing rate map, autocorrelation matrix for rate map, coverage heat map based on the position of the animal, smoothed polar histogram of head direction when the cell fired (red, Hz) and from the whole session (black), scatter plot of firing events colour-coded for head direction on trajectory. Third row left to right: Detected firing fields on rate map and polar histograms of head direction in detected fields. The animal ID is indicated above the plots.
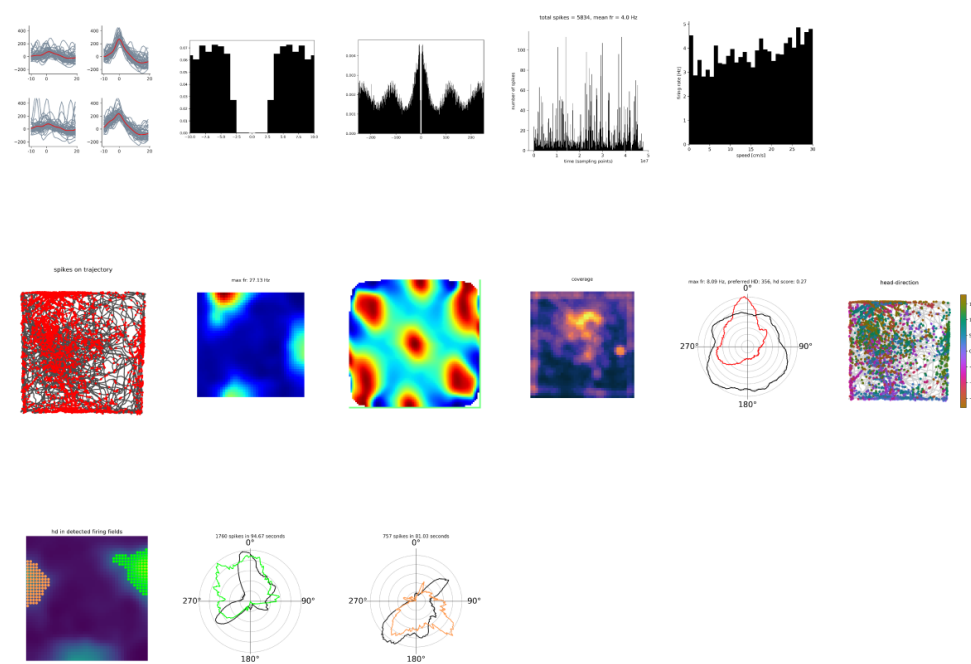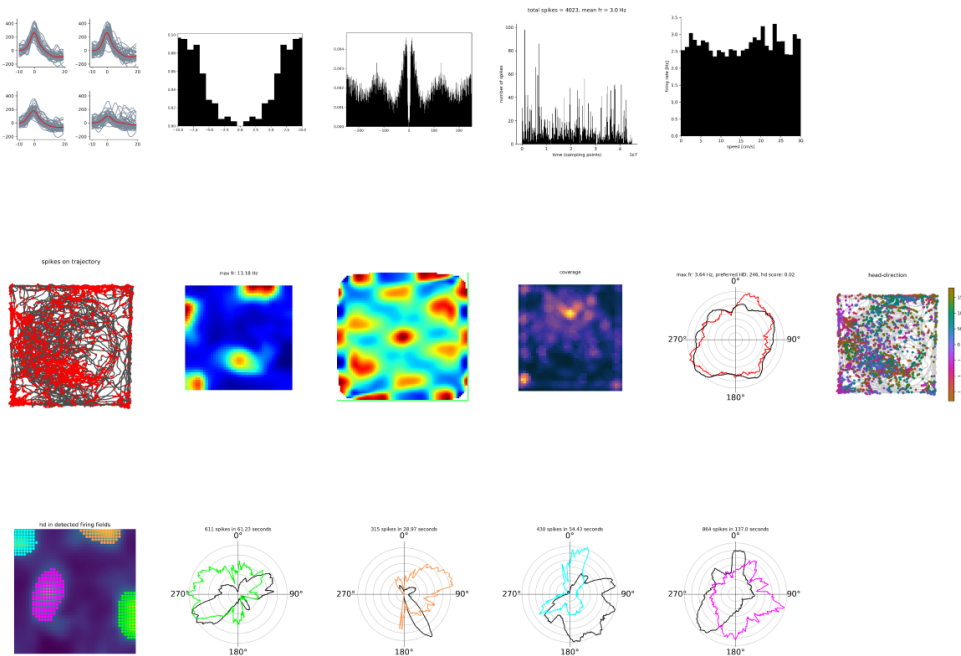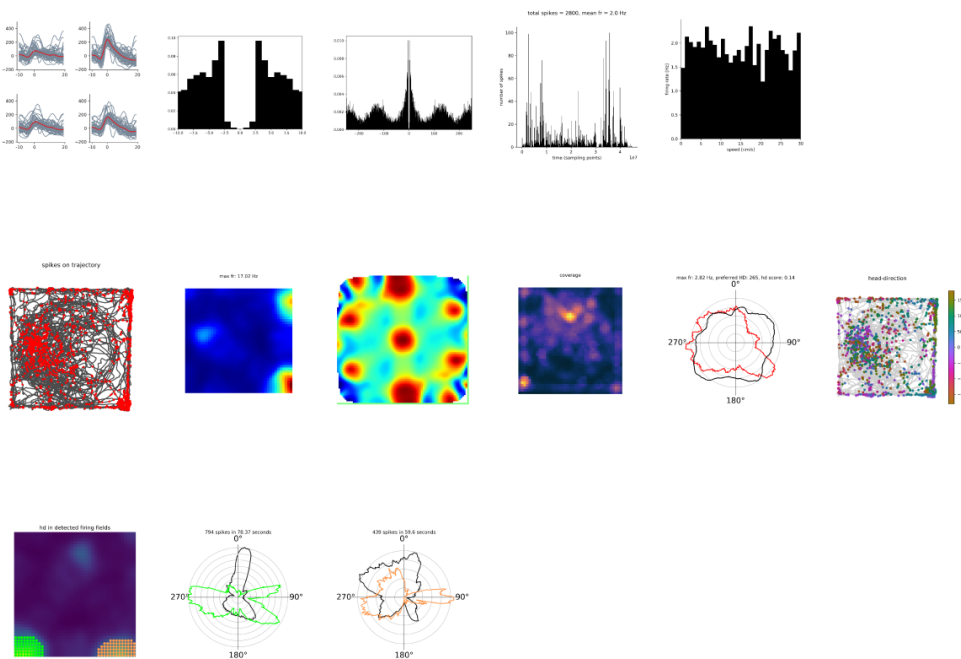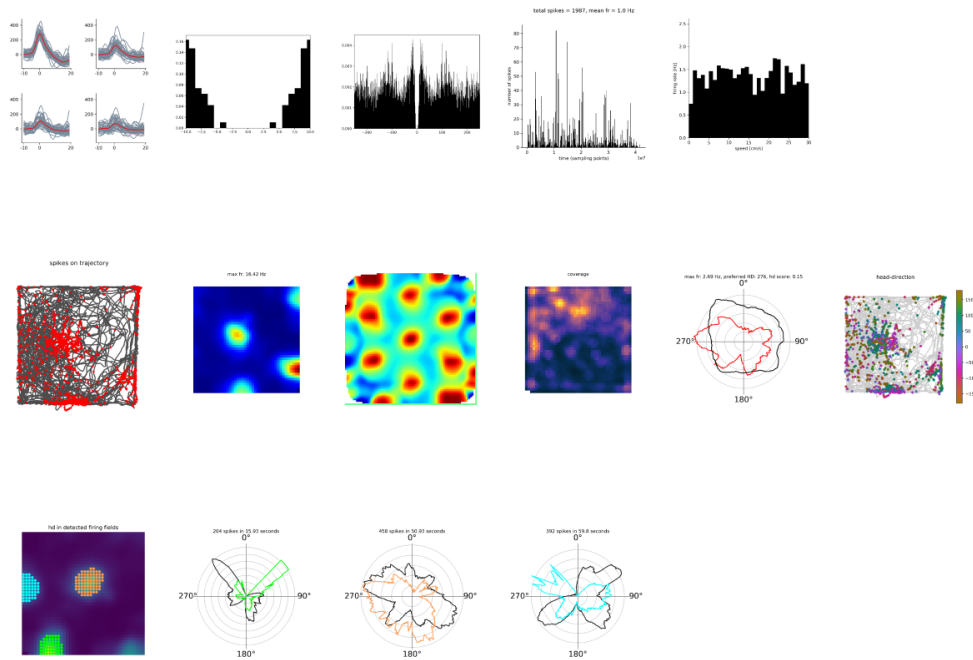
Grid cells

F

F

F

F

F

51
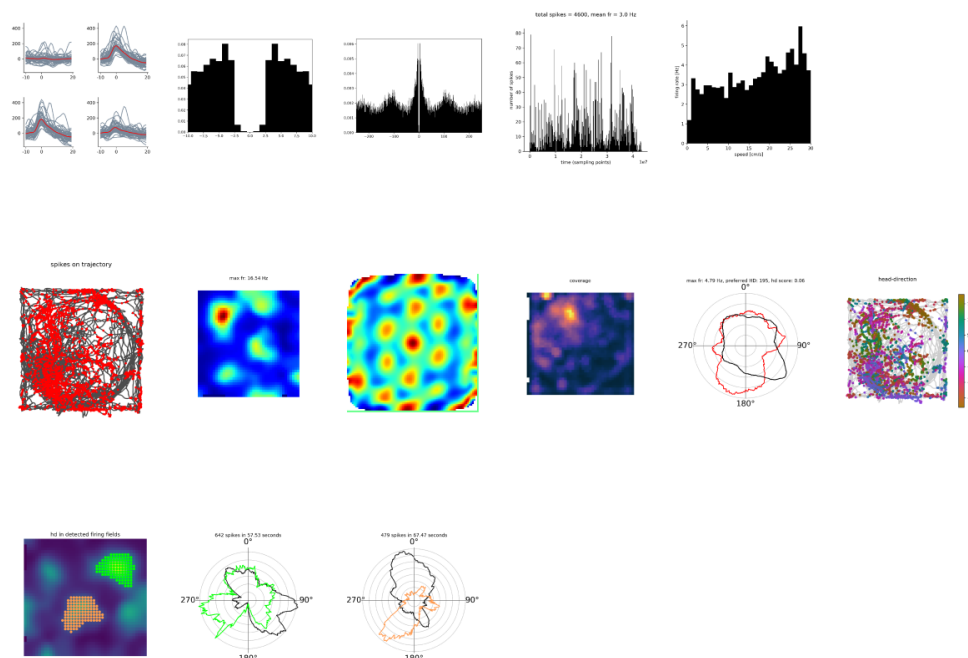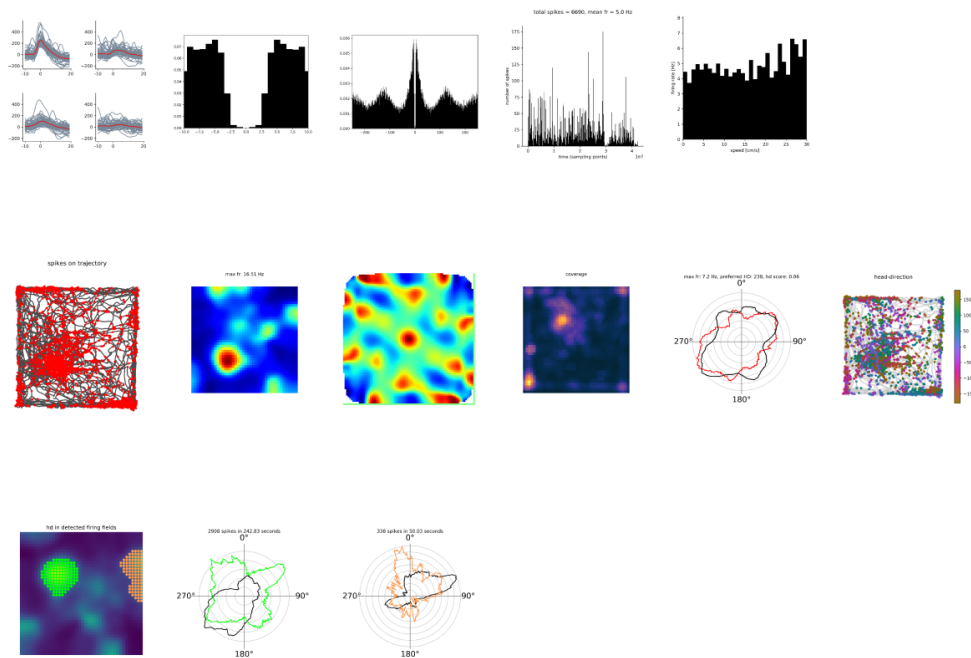
F

F
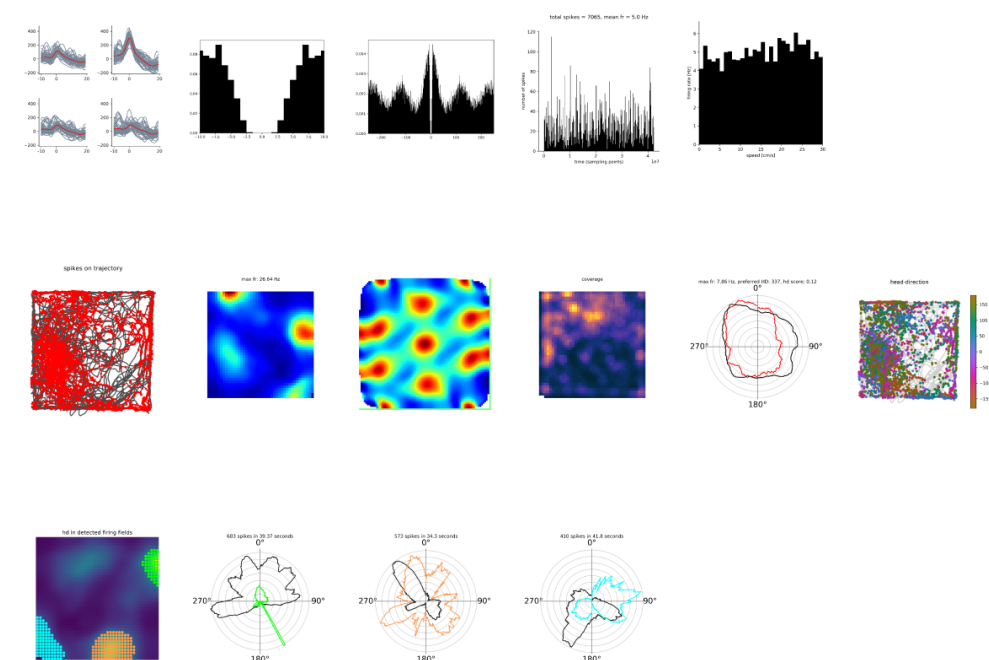
F
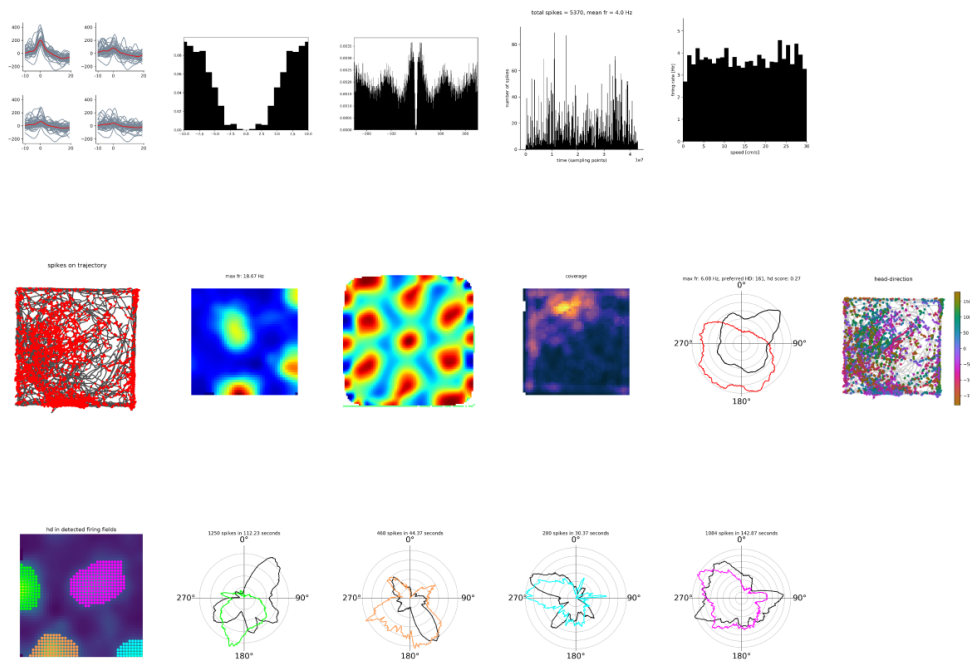
F
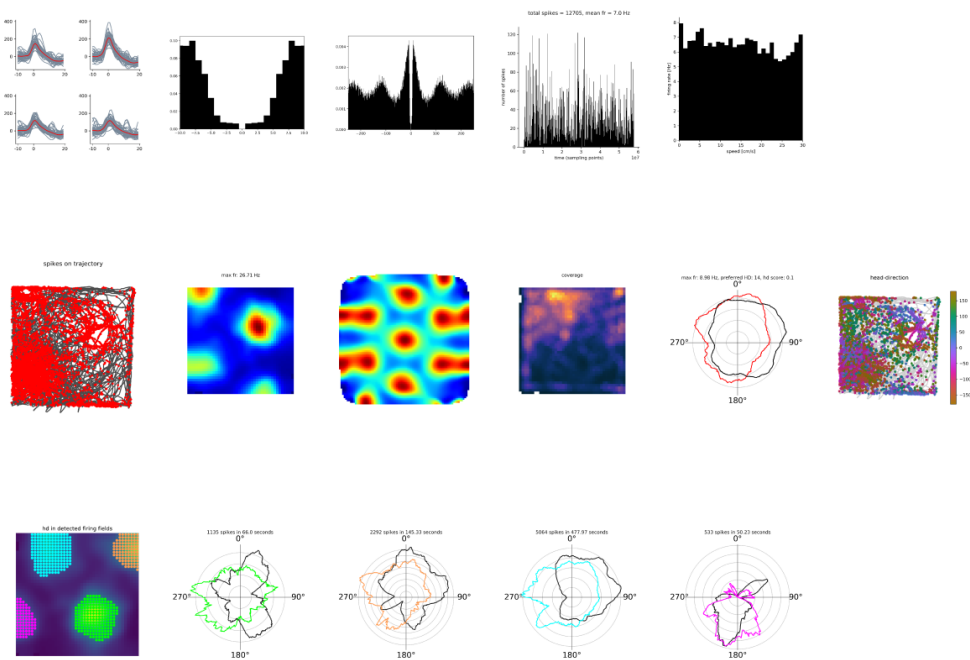
K
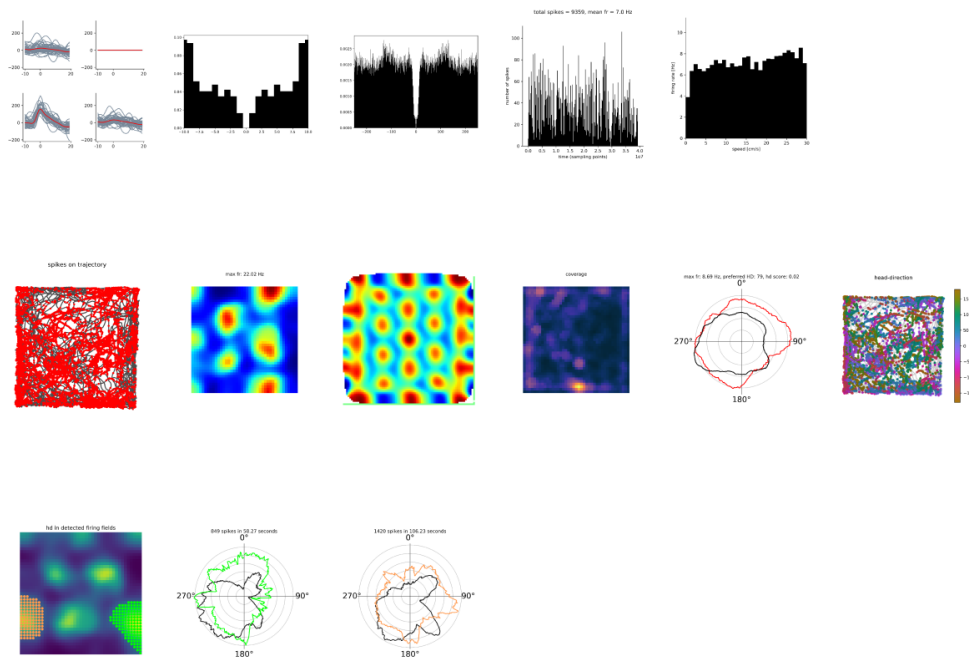
K

K

L

M

References

1. Bellmund, J. L. S., Gärdenfors, P., Moser, E. I. & Doeller, C. F. Navigating cognition: Spatial codes for human thinking. *Science* **362**, (2018).
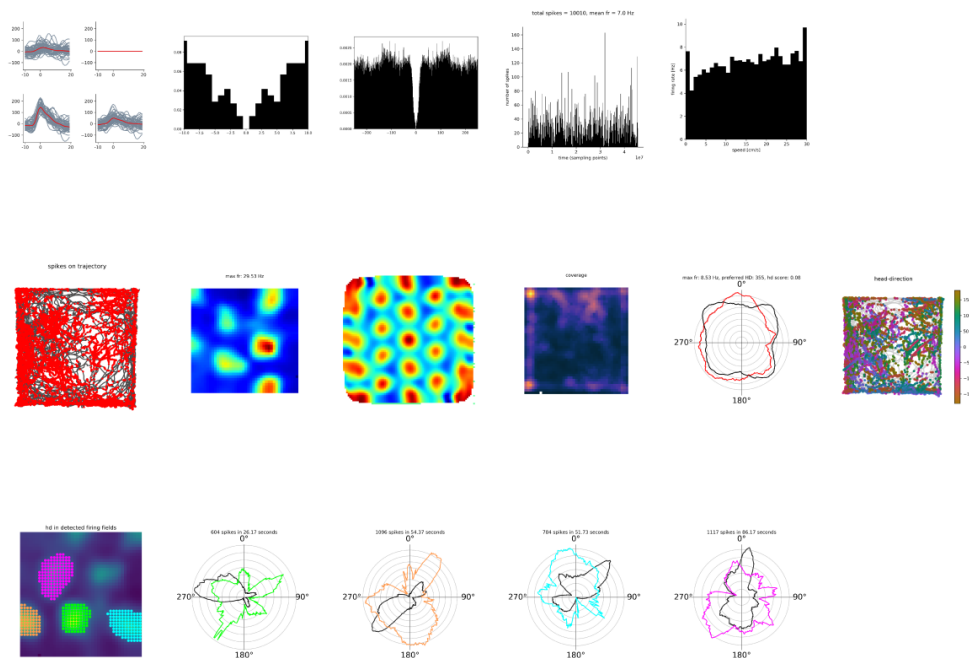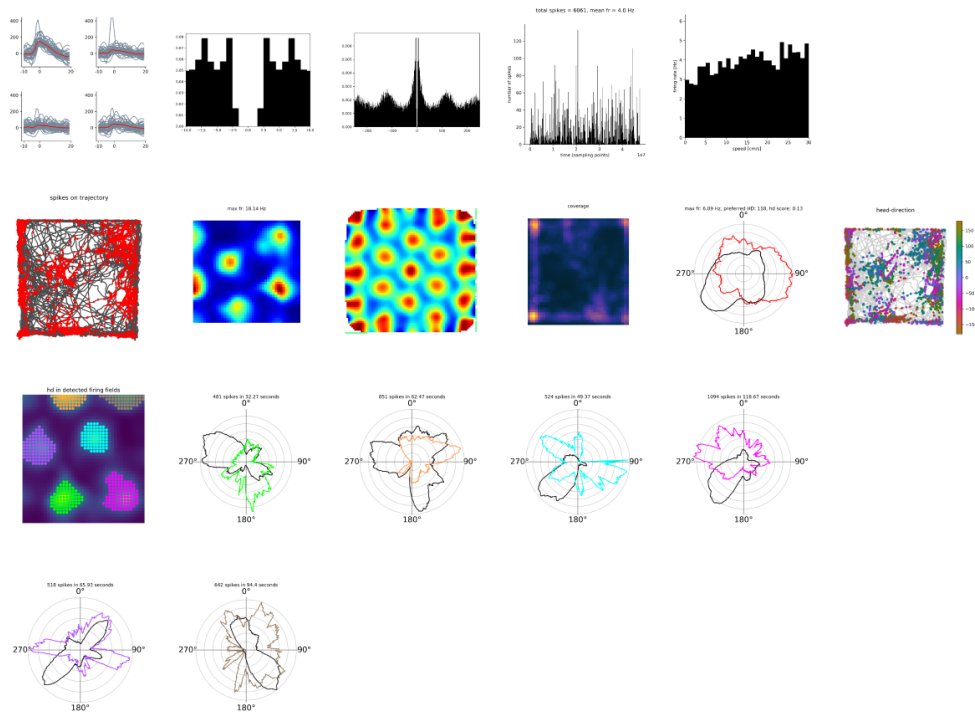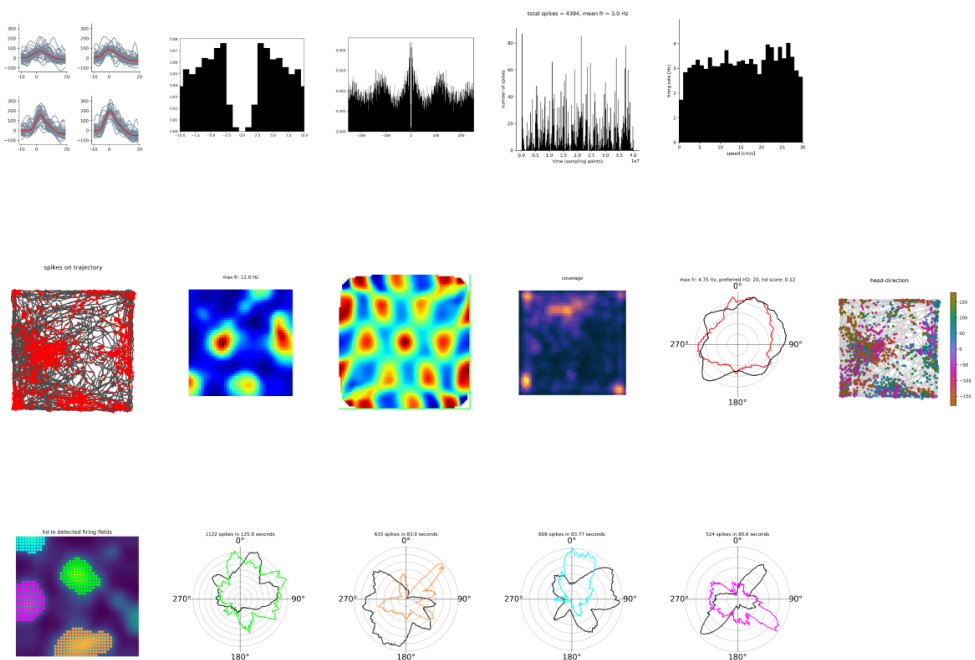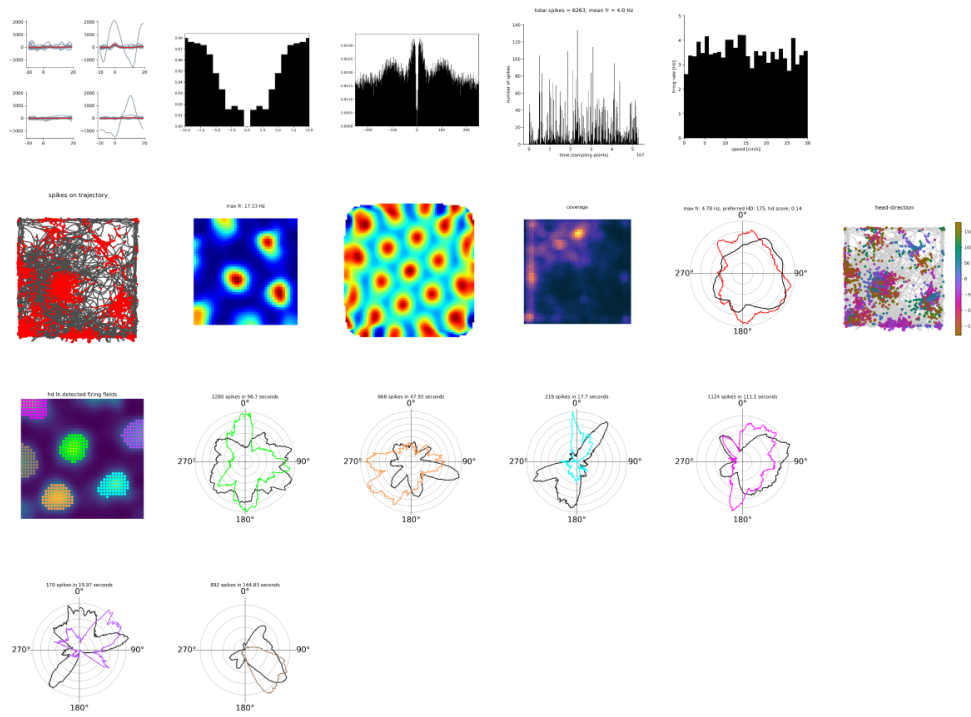
2. Moser, E. I., Moser, M.-B. & McNaughton, B. L. Spatial representation in the hippocampal formation: a history. *Nat. Neurosci.* **20**, 1448–1464 (2017).

3. Sargolini, F. *et al.* Conjunctive representation of position, direction, and velocity in entorhinal cortex. *Science* **312**, 758–762 (2006).

4. McNaughton, B. L., Battaglia, F. P., Jensen, O., Moser, E. I. & Moser, M.-B. Path integration and the neural basis of the 'cognitive map'. *Nat. Rev. Neurosci.* **7**, 663–678 (2006).

5. Burak, Y. & Fiete, I. R. Accurate path integration in continuous attractor network models of grid cells. *PLoS Comput. Biol.* **5**, e1000291–e1000291 (2009).

6. Fiete, I. R., Burak, Y. & Brookings, T. What grid cells convey about rat location. *J. Neurosci.* **28**, 6858–6871 (2008).

7. Stemmler, M., Mathis, A. & Herz, A. V. M. Connecting multiple spatial scales to decode the population activity of grid cells. *Science Advances* **1**, e1500816–e1500816 (2015).

8. Guanella, A., Kiper, D. & Verschure, P. A model of grid cells based on a twisted torus topology. *Int. J. Neural Syst.* **17**, 231–240 (2007).

9. Burgess, N., Barry, C. & O'Keefe, J. An oscillatory interference model of grid cell firing. *Hippocampus* **17**, 801–812 (2007).

10. Fuhs, M. C. & Touretzky, D. S. A spin glass model of path integration in rat medial entorhinal cortex. *J. Neurosci.* **26**, 4266–4276 (2006).

11. Bush, D., Barry, C., Manson, D. & Burgess, N. Using Grid Cells for Navigation. *Neuron* **87**, 507–520 (2015).

12. Leutgeb, J. K., Leutgeb, S., Moser, M.-B. & Moser, E. I. Pattern separation in the dentate gyrus and CA3 of the hippocampus. *Science* **315**, 961–966 (2007).

13. Knierim, J. J. & Neunuebel, J. P. Tracking the flow of hippocampal computation: Pattern separation, pattern completion, and attractor dynamics. *Neurobiol. Learn. Mem.* **129**, 38–49 (2016).

14. Cayco-Gajic, A. N. & Silver, A. R. Re-evaluating Circuit Mechanisms Underlying Pattern Separation. *Neuron* **101**, 584–602 (2019).

15. Hafting, T., Fyhn, M., Molden, S., Moser, M.-B. & Moser, E. I. Microstructure of a spatial map in the entorhinal cortex. *Nature* **436**, 801–806 (2005).

16. Constantinescu, A. O., O'Reilly, J. X. & Behrens, T. E. J. Organizing conceptual knowledge in humans with a gridlike code. *Science* **352**, 1464–1468 (2016).

17. Hardcastle, K. *et al.* A Multiplexed , Heterogeneous , and Adaptive Code for Navigation in Medial Entorhinal Cortex. *Neuron* 1–13 (2017).

18. Pastoll, H., Solanka, L., van Rossum, M. C. W. & Nolan, M. F. Feedback Inhibition Enables Theta-Nested Gamma Oscillations and Grid Firing Fields. *Neuron* **77**, 141–154 (2013).

19. Muller, R. U., Bostock, E., Taube, J. S. & Kubie, J. L. On the directional firing properties of hippocampal place cells. *J. Neurosci.* **14**, 7235–7251 (1994).

20. Giocomo, L. M., Moser, M.-B. & Moser, E. I. Review Computational Models of Grid Cells. *Neuron* **71**, 589–603 (2011).

21. Tocker, G., Barak, O. & Derdikman, D. Grid cells correlation structure suggests organized feedforward projections into superficial layers of the medial entorhinal cortex. *Hippocampus* (2015). doi:10.1002/hipo.22481

22. Ismakov, R., Barak, O., Jeffery, K. & Derdikman, D. Grid Cells Encode Local Positional Information. *Curr. Biol.* **27**, 2337–2343.e3 (2017).

23. Beed, P. *et al.* Analysis of excitatory microcircuitry in the medial entorhinal cortex reveals cell-type-specific differences. *Neuron* **68**, 1059–1066 (2010).

24. Sürmeli, G. *et al.* Molecularly Defined Circuitry Reveals Input-Output Segregation in Deep Layers of the Medial Entorhinal Cortex. *Neuron* **88**, 1040–1053 (2015).

25. Garden, D. L. F., Dodson, P. D., O'Donnell, C., White, M. D. & Nolan, M. F. Tuning of synaptic integration in the medial entorhinal cortex to the organization of grid cell firing fields. *Neuron* **60**, 875–889 (2008).

26. Samsonovich, A. & McNaughton, B. L. Path integration and cognitive mapping in a continuous attractor neural network model. *J. Neurosci.* **17**, 5900–5920 (1997).

27. Hardcastle, K., Ganguli, S. & Giocomo, L. M. Cell types for our sense of location: where we are and where we are going. *Nat. Neurosci.* **20**, 1474–1482 (2017).

28. Tennant, S. A. *et al.* Stellate Cells in the Medial Entorhinal Cortex Are Required for Spatial Learning. *Cell Rep.* **22**, 1313–1324 (2018).

29. Qin, H. *et al.* A Visual-Cue-Dependent Memory Circuit for Place Navigation. *Neuron* 1–9 (2018).

30. Gu, Y. *et al.* A Map-like Micro-Organization of Grid Cells in the Medial Entorhinal Cortex. *Cell* **175**, 736–750.e30 (2018).

31. Doeller, C. F., Barry, C. & Burgess, N. Evidence for grid cells in a human memory network. *Nature* **463**, 657–661 (2010).

32. Killian, N. J., Jutras, M. J. & Buffalo, E. a. A map of visual space in the primate entorhinal cortex. *Nature* **5**, 3–6 (2012).

33. Shima, Y. *et al.* A Mammalian enhancer trap resource for discovering and manipulating neuronal cell types. *Elife* **5**, e13503 (2016).

34. Anikeeva, P. *et al.* Optetrode: a multichannel readout for optogenetic control in freely moving mice. *Nat. Neurosci.* **15**, 163–170 (2011).

35. Grieves, R. M., Jenkins, B. W., Harland, B. C., Wood, E. R. & Dudchenko, P. A. Place field repetition and spatial learning in a multicompartment environment. *Hippocampus* **26**, 118–134 (2016).

36. Lopes, G. *et al.* Bonsai: an event-based framework for processing and controlling data streams. *Frontiers in Neuroinformatics* **9**, (2015).

37. Siegle, J. H. *et al.* Open Ephys: an open-source, plugin-based platform for multichannel electrophysiology. *J. Neural Eng.* **14**, 045003 (2017).

38. Chung, J. E. *et al.* A Fully Automated Approach to Spike Sorting. *Neuron* **95**, 1381–1394.e6 (2017).

39. Krupic, J., Bauza, M., Burton, S., Barry, C. & O'Keefe, J. Grid cell symmetry is shaped by environmental geometry. *Nature* **518**, 232–235 (2015).

40. Harvey, C. D., Collman, F., Dombeck, D. A. & Tank, D. W. Intracellular dynamics of hippocampal place cells during virtual navigation. *Nature* **461**, 941–946 (2009).

41. Fernández-Durán, J. J. & Domínguez, M. M. G.-. A Likelihood Ratio Test for Homogeneity in Circular Data. *Journal of Biometrics & Biostatistics* (2010). doi:10.4172/2155-6180.1000107

42. Pewsey, A., Neuhäuser, M. & Ruxton, G. D. *Circular Statistics in R*. (OUP Oxford, 2013).

43. Hines, M. L. & Carnevale, N. T. The NEURON simulation environment. *Neural Comput.* **9**, 1179–1209 (1997).

44. Mainen, Z. F. & Sejnowski, T. J. Influence of dendritic structure on firing pattern in model neocortical neurons. *Nature* **382**, 363–366 (1996).

45. Nolan, M. F., Dudman, J. T., Dodson, P. D. & Santoro, B. HCN1 channels control resting and active integrative properties of stellate cells from layer II of the entorhinal cortex. *J. Neurosci.* **27**, 12440–12451 (2007).

46. Pastoll, H., Ramsden, H. L. & Nolan, M. F. Intrinsic electrophysiological properties of entorhinal cortex stellate cells and their contribution to grid cell firing fields. *Front. Neural Circuits* **6**, 1–21 (2012).

47. Giocomo, L. M., Zilli, E. A., Fransén, E. & Hasselmo, M. E. Temporal frequency of subthreshold oscillations scales with entorhinal grid cell field spacing. *Science* **315**, 1719–1722 (2007).

48. Kropff, E. & Treves, A. The emergence of grid cells: Intelligent design or just adaptation?

Hippocampus **18**, 1256–1269 (2008).

49. Mirowski, P. *et al.* Learning to Navigate in Complex Environments. (2016).

50. Milford, M. J., Wiles, J. & Wyeth, G. F. Solving navigational uncertainty using grid cells on robots. *PLoS Comput. Biol.* **6**, e1000995–e1000995 (2010).

51. Banino, A. *et al.* Vector-based navigation using grid-like representations in artificial agents. *Nature* **557**, 429–433 (2018).